Spatial and temporal heterogeneity in bevacizumab treated breast tumors resolved by eigenspectra Multispectral Optoacoustic Tomography

Evangelos Liapis[1*], Uwe Klemm[1], Angelos Karlas[1,2], Josefine Reber[1] and Vasilis Ntziachristos[1,2]

[1]Institute of Biological and Medical Imaging, Helmholtz Zentrum München, Munich, Neuherberg 85764, Germany.

[2]Chair of Biological Imaging, TranslaTUM Technical University of Munich, Ismaningerstr. 22, Munich 81675, Germany

***Corresponding Author:** evagelos2005@hotmail.com

Running Title: eMSOT-resolved oxygenation in bevacizumab treated tumors

Keywords: Optoacoustic; Photoacoustic; Tumor; Hypoxia; Bevacizumab

Additional information

Financial Support

The study was supported by a grant from Sonderforschungsbereich-824 (SFB-824), subproject A1.

Disclosure of Potential Conflicts of Interest

V. Ntziachristos holds ownership interest (including patents) in iThera Medical GmbH. No potential conflicts of interest were disclosed by the other authors.

Word count: 4562. **Total number of Figures and Tables:** 7

Abstract

Understanding temporal and spatial hemodynamic heterogeneity as a function of tumor growth or therapy has impact on the development of novel therapeutic strategies. We employed eigenspectra multispectral optoacoustic tomography (eMSOT) as a next-generation optoacoustic method to impart high accuracy in resolving tumor hemodynamics during bevacizumab therapy in two types of breast cancer xenografts (KPL-4, MDA-MB-468). We imaged patterns of tumor total hemoglobin concentration (THb) and oxygen saturation (sO_2) in control and bevacizumab treated tumors over the course of 58d (KPL-4) and 16d (MDA-MB-468) and resolved macroscopically the evolution of functional vasculature “normalization”. We observed an initial sharp drop in tumor sO_2 and THb content shortly after the initiation of bevacizumab treatment followed by a recovery in oxygenation levels. Rim-core subregion analysis revealed steep spatial oxygenation gradients in growing tumors that were reduced after bevacizumab treatment. Critically, eMSOT imaging findings were validated directly by histopathologic assessment of hypoxia (pimonidazole) and vascularity (CD31). We demonstrate how eMSOT brings new abilities for accurate observation of entire tumor responses to challenges at spatial and temporal dimensions, not available by other techniques today.

Significance: Accurate assessment of hypoxia and vascularization over space and time is critical for understanding tumor development and the role of spatial heterogeneity in tumor aggressiveness, metastasis and response to treatment.

Introduction

Multispectral optoacoustic tomography (MSOT) provides 3D anatomical, functional and molecular information by resolving the distribution of endogenous or exogenously-administered light-absorbing molecules in tissue based on their absorption spectral signatures (1). MSOT provides label free measurements of total hemoglobin concentration (THb) and hemoglobin oxygen saturation (sO_2) in tissue and can also sense contrast from melanin, water and lipid content. Consequently, the technique has been used to study oxygenation and vascularity of animal tumors (2-4) and in clinical settings resolving oxygenation, inflammation, and metabolism in label-free mode (5-9). Anticancer therapies have also been studied by MSOT imaging; examples include photodynamic therapy (10), vascular disrupting agents (3) and antiangiogenics (11). Nevertheless, MSOT and optoacoustics in general, has not yet been rigorously validated against gold histologic standards as to its ability to visualize spatiotemporally heterogeneous patterns of tumor oxygenation and vascularization. Moreover, none of the published studies has accounted for the strong, non-linear dependence of photon fluence on depth and on wavelength, which leads to spectral coloring and challenges the accuracy achieved, especially as the depth of the observations increases. We have previously introduced a new class of methods, termed eigenspectra multispectral optoacoustic tomography (eMSOT), based on the eigenvalue decomposition of the spectral unmixing problem (12,13), with documented superior performance to linear unmixing methods utilized so far. eMSOT provides substantially improved quantification of oxygenation compared to conventional spectral unmixing schemes by solving the spectral unmixing problem in the spectral domain instead of the spatial domain; an effective way to account for the effects of depth and optical properties on the optoacoustic spectra. eMSOT therefore holds great potential in quantification of tumor oxygenation, especially in response to anticancer regimens.

Antiangiogenic treatment is typically applied in combination with chemotherapy over the course of several months; however, little is known regarding the spatial and functional modification of the tumor environment during the therapeutic course. The effects of the prototypical antiangiogenic drug bevacizumab (Avastin) (14) on tumor microvasculature are well described and have been studied in both animals and humans by histologic analysis (15,16), ex-vivo imaging (17,18) and intravital microscopy (19-22). Macroscopically, the antivascular effects of bevacizumab therapy have been investigated using a number of non-invasive imaging modalities, including computed tomography (CT) (23), dynamic contrast-enhanced ultrasonography (DCE-US) (24), and dynamic contrast enhanced MRI (DCE-MRI) (for relevant reviews, see (25-28)). However, the functional consequences of bevacizumab therapy on tumor vasculature and oxygenation are still controversial and appear to be dependent on several factors, including dosage, treatment duration and scheduling, method of detection and experimental tumor model used (28). Accordingly, several preclinical studies in animal tumors documented elevations in tumor oxygenation (16,29-31), whereas others reported increased intratumoral hypoxia (32-34) after the first few days of treatment with bevacizumab. The results from clinical studies in glioblastoma and breast cancer patients receiving bevacizumab therapy are equally contradictory, with some studies describing improvements in tumor oxygenation based on [^{18}F]fluoromisonidazole (FMISO) PET (35,36) or histology (37,38), and others reporting increases in intratumoral hypoxia based on FMISO uptake and/or diffuse optical spectroscopic imaging (DOSI) (39,40) and dynamic susceptibility contrast MRI (DSC-MRI) (41). Given the ability of eMSOT to provide accurate oxygenation readings at high spatiotemporal resolution and increased imaging depths, we hypothesized that longitudinal eMSOT imaging would offer valuable insights into the dynamics and spatial distribution of breast tumor oxygenation along the course of bevacizumab therapy.

The present study had two major aims. The first one was to resolve breast tumor hemodynamics during *de novo* growth and also over the course of bevacizumab therapy, using eMSOT imaging in a longitudinal fashion. To accomplish this, we employed two breast xenograft models (KPL-4, MDA-MB-468). The two models are representative of human HER2-enriched (KPL-4) and triple negative (MDA-MB-468) breast cancer and their responsiveness to bevacizumab therapy has been previously confirmed (42,43). Although both types of xenografts model breast cancer at an advanced stage, we demonstrate that MDA-MB-468 tumors exhibit considerably faster growth kinetics and higher microvascular density compared to KPL-4, in line with the well-known aggressive growth of triple negative breast tumors. The second aim was to validate our *in vivo* eMSOT findings, using a rigorous scheme consisting of 1) precise alignment and registration of optoacoustic tumor planes with corresponding whole tumor cryosections, and 2) immunohistochemical staining against markers of hypoxia (pimonidazole), vascularity (CD31) and perivascular coverage (α-SMA). In addition, in order to assess the spatial heterogeneity in tumor oxygenation and functional vascularization we performed a differential analysis of hemodynamic responses at the core and rim tumor regions similarly to previous studies (2,44,45). Lastly, to obtain a more complete *in vivo* mapping of the functional macrovascular network we conducted a 3D morphometry analysis based on THb signal. Our work paves the way for longitudinal, non-invasive assessment of tumor hemodynamic response to therapy.

Materials and Methods

Compounds

Clinical grade bevacizumab (Avastin®; Roche, Basel, Switzerland) was obtained as a stock solution of 25 mg/mL and was diluted with sterile saline (B.Braun, Germany).

Cell lines

The human breast adenocarcinoma cell line KPL-4 was kindly provided by J. Kurebayashi (Kawasaki Medical School, Kurashiki, Japan). KPL-4 cells were cultured in Dulbecco's modified Eagle's medium (Sigma). The human breast adenocarcinoma cell line MDA-MB-468 was kindly provided by S. Stangl (Klinik und Poliklinik für Strahlentherapie und Radiologische Onkologie, TUM, Munich, Germany). MDA-MB-468 cells were cultured in RPMI-1640 medium (Sigma). Both culture media were supplemented with 10% FBS (Gibco) and 1% pen strep (Sigma). Cells were cultured at 37°C and 5% CO_2 and routinely passaged twice weekly until they reached the final cell concentration for injection.

Experimental Model

A general overview of the experimental workflow and data analysis followed in the present study is shown in Figure 1. The inhibitory effects of bevacizumab on tumor oxygenation and vascularity were tested on two well-established estrogen-independent breast tumor models that are commonly used in therapeutic studies: the human HER2-overexpressing KPL-4 (42,46) and the triple-negative MDA-MB-468 (47) mammary adenocarcinoma cell lines (Fig. 1A). These cell lines were implanted orthotopically into the 3rd thoracic mammary fat pads of hairless NOD.SCID mice, with a tumor take of 100%. Following implantation, the tumors were allowed to grow to an average volume of ≈ 200-250 mm^3 before initiating bevacizumab treatment

(Fig. 1B). Treatment was initiated immediately following the first MSOT imaging session. MSOT imaging was performed by acquiring transversal multispectral optoacoustic slices spaced by 300 µm across the entire tumor volume (Fig. 1C). Next, optoacoustic images were reconstructed (Fig. 1D), processed using the eMSOT algorithm (Fig. 1E) and measurements were extracted in the form of oxygen saturation (sO_2) and total hemoglobin (THb) concentration. These metrics were quantified in three tumor regions (whole tumor, rim, core) by subregion segmentation analysis (Fig. 1F). Rim-core segmentation of eMSOT-sO_2 and THb images was performed in ImageJ (imageJ.nih.gov) by manually tracing ROIs encompassing each tumor subregion. Rim was defined as the perimeter area of 1 mm depth into the tumor for tumors < 1 cm in diameter and of 2 mm depth in tumors > 1 cm in diameter. Core was defined as the remaining tumor area after the rim was excluded. Rim-core subregion analysis was performed using the 10 most central optoacoustic sections of each tumor. After the final MSOT imaging session, mice were sacrificed and tumors were harvested for cryoslicing (Fig. 1G) and immunohistological analysis against CD31, pimonidazole and α-SMA (Fig. 1H). Bevacizumab treatment and MSOT imaging scheduling of KPL-4 and MDA-MB-468 tumors are shown in Figs. 1I-J, respectively.

Statistical analysis

Statistical analyses of data were performed using Graphpad Prism 6 (GraphPad Software, San Diego, CA) and graphical representation using Prism and Microsoft Excel (Microsoft, WA, USA). For each optoacoustic imaging experiment, a representative of three independent experiments is presented in this work. All results in this work are reported as mean ± S.E.M., except for tumor growth and weight curves which were reported as mean ± SD. For time point comparisons of the mean difference in whole tumor sO_2 and THb within a single tumor type, two-tailed paired t test was performed. Two-tailed unpaired t test was used for time endpoint comparisons between different tumor types (KPL-4 vs MDA-MB 468). For temporal variations in rim-core oxygenation and vascularity within a single treatment group one-way ANOVA test was performed. P values of < 0.05 were considered statistically significant. Correlations between eMSOT-derived mean core sO_2 and pimonidazole-determined HF were assessed on a per-tumor basis by two-tailed Pearson correlation analysis using pooled HF and eMSOT-core sO_2 measurements from KPL-4 (n = 9) and MDA-MB-468 (n = 5) tumors of control and bevacizumab treated mice for which co-registration of optoacoustic and histologic image pairs was possible. Correlations between CD31+ MVD and CD31+ VF were assessed on a per slide basis by two-tailed Pearson correlation analysis using pool data from KPL-4 (n = 49 slides) and MDA-MB-468 (n = 24 slides) tumors of control and bevacizumab treated mice.

Detailed procedures for MSOT imaging, eMSOT image processing, 3D morphometric analysis of functional macrovasculature, histopathologic tumor analysis, optoacoustic and histological image registration, and calculation of hypoxic, necrotic/vascular fractions, microvessel density (MVD) and pericyte coverage are described in Supplementary Methods.

Results

Bevacizumab delays KPL-4 and MDA-MB-468 tumor growth

In KPL-4 tumor-bearing mice, bevacizumab treatment induced a tumor growth inhibition (TGI) of 32% and a prolonged growth delay of 24 days compared to controls (Fig. 1K). Furthermore, all 7 tumors from bevacizumab treated mice responded to the treatment, as shown in the individual tumor growth curves from each group (Supplementary Fig. S2A-B) and the tumor photographs obtained at the end of the experiment (Supplementary Fig. S2E). MDA-MB-468 tumors from control mice (Fig. 1L) exhibited significantly faster growth kinetics than respective KPL-4 controls. Analogously to KPL-4, the mean MDA-MB-468 tumor volume was significantly lower in the bevacizumab group ($p = 0.006$) at the end of treatment (d37 post implantation (p.i.)), displaying a TGI of 47% and a growth delay of 10 days when compared with the control group. No loss of animal body weight or morbidity was observed in mice bearing KPL-4 or MDA-MB-468 tumors treated with either vehicle or bevacizumab at this dosage and schedule throughout the duration of the experiments (Supplementary Fig. S1).

Bevacizumab reduces functional neovascularization in KPL-4 and MDA-MB 468 xenografts

We applied MSOT to examine trends in functional neovascularization patterns occurring during physiologic tumor growth (control group), as well as in response to bevacizumab therapy. Quantification of mean whole tumor THb signal showed relatively stable THb levels in control MDA-MB-468 tumors throughout the imaging course (Fig. 3A). However, in KPL-4 controls (Fig. 2A) the mean whole tumor blood volume decreased significantly during the observation period ($p = 0.031$). MSOT imaging revealed a sharp drop in the THb content of both KPL-4 (Fig. 2A) and MDA-MB-468 (Fig. 3A) tumors shortly after bevacizumab administration. The profound reduction in THb content in tumors of bevacizumab treated animals is also evident in the series of MSOT images (Figs. 2C-D, 3C-D and Supplementary Figs. S3-4). The mean whole tumor THb remained significantly lower in bevacizumab compared to vehicle treated animals until the end of therapy in MDA-MB-468 (Fig.3A), while in

KPL-4 tumors the gap in THb between the groups narrowed considerably towards the end of the imaging experiment (Fig. 2A).

Bevacizumab induces a biphasic oxygenation response in KPL-4 and MDA-MB-468 tumor xenografts

Analysis of temporal whole tumor sO_2 trends showed that in control mice the oxygenation dynamics differed considerably between the two breast cancer models during the course of the imaging study (Figs. 2B, 3B). Specifically, KPL-4 control tumors displayed a sudden increase in mean sO_2 levels over the first 5 days of MSOT imaging, after which sO_2 levels plateaued (Fig. 2B). On the other hand, MDA-MB-468 tumors from control mice showed little temporal variation in mean sO_2 values over the observation window (Fig. 3B).

Both tumor models exhibited a similar dynamic response to bevacizumab treatment, characterized by an initial acute hypoxic response followed by a gradual increase in mean whole tumor sO_2 levels over time (Figs. 2-3 and Supplementary Figs. S3-4). In KPL-4 tumors, a sharp and significant drop in KPL-4 tumor oxygenation was detected in bevacizumab treated mice 2 days post treatment (Fig. 2B), which is also visible in the parametric eMSOT sO_2 maps (lower panels, Figs. 2C-D). From d2 onwards, the average KPL-4 tumor sO_2 progressively increased, although sO_2 was not restored to pre-treatment levels until d45 (Fig. 2B). At the end time point of the MSOT imaging experiment (d58), mean whole KPL-4 tumor sO_2 levels in the bevacizumab group were significantly higher than baseline pre-treatment levels ($p = 0.028$) and marginally lower than those detected in control mice (Fig. 2B). Inter-tumoral variation in sO_2 over time was relatively low, as can be seen in the individual sO_2 curves for control (Supplementary Fig. S2C) and bevacizumab (Supplementary Fig. S2D) KPL-4 treatment groups.

A similar but less pronounced temporal trend in sO_2 values was detected in MDA-MB-468 tumors of the bevacizumab group (Fig. 3B), which displayed a distinct drop in mean sO_2 shortly after bevacizumab administration (d2), after which whole tumor oxygenation was quickly (d11) restored to pre-treatment levels (Fig. 3B).

Bevacizumab reduces blood volume primarily at the rims of KPL-4 and MDA-MB-468 tumors

By sampling subregions within tumors we were able to monitor the spatial heterogeneity in functional vascularization of KPL-4 and MDA-MB 468 tumors from mice undergoing vehicle or bevacizumab treatment. The mean THb content at the rim subregion of control KPL-4 and MDA-MB-468 tumors remained relatively constant throughout the imaging period, while core THb declined over time in both tumor types, particularly in KPL-4 (Figs. 4A-B and Supplementary Table S1).

The inhibitory effects of bevacizumab therapy on functional tumor vasculature were more prominent at the periphery than at core regions of KPL-4 and MDA-MB-468 tumors (Figs. 4A-B). Rim THb levels became significantly lower in the bevacizumab group shortly after the onset of treatment in both tumor models (black asterisks, Figs. 4A-B) and remained lower than corresponding controls until the end of each time course. Accordingly, 3D morphometric analysis of the extracted functional macrovasculature revealed that bevacizumab treatment induced substantial reductions in the overall length and branching density of the strongly enhanced macroscopic tumor vessel network (Figs. 7A-C and Supplementary Fig. 6A).

On the other hand, the effects of bevacizumab therapy on intratumoral (core) THb content were less noticeable. In KPL-4, bevacizumab treatment induced a transient but significant drop in THb at the tumor core that peaked on d24 (green asterisk, Fig.

4A), while in MDA-MB-468 tumors, core THb was virtually identical between the two groups throughout the imaging period (Fig. 4B).

Bevacizumab improves intratumoral sO_2 and reduces the spatial heterogeneity in oxygenation of KPL-4 and MDA-MB-468 tumors

Quantification of sO_2 levels at the rim and core regions of KPL-4 (Fig. 4C) and MDA-MB-468 (Fig. 4D) tumors revealed significant differences in the spatiotemporal distribution of oxygenation between the two treatment groups (Figs. 4C-D), as well as within each single treatment group (Figs. 4E-H).

Starting with the tumor rim subregion, eMSOT imaging revealed a sharp drop in rim sO_2 levels shortly after initiation of bevacizumab therapy, regardless of tumor type (black asterisks, Figs. 4C-D). Oxygen saturation levels remained significantly lower at the tumor rims of bevacizumab treated animals until the end of therapy in MDA-MB-468 (Fig. 4D), whereas in KPL-4, rim sO_2 was comparable between the groups by the end of treatment (d58, Fig. 4C). Similarly, an acute drop in intratumoral (core) sO_2 was observed immediately after the onset of bevacizumab therapy, particularly in KPL-4 tumors (Figs. 4C-D). However, following this initial drop, core sO_2 in the bevacizumab group remained relatively stable, whereas in controls it declined over time and as such, by the end of treatment, intratumoral sO_2 levels were considerably higher in bevacizumab treated mice, particularly in the MDA-MB-468 model (green asterisks, Fig. 4C-D).

The spatiotemporal sO_2 distribution within each single treatment group is better illustrated in the bar graph representations of the same dataset (Figs. 4E-H). Intratumoral hypoxia developed faster and was more severe in MDA-MB-468 (Fig. 4G) compared to KPL-4 (Fig. 4E) control tumors. On the other hand, bevacizumab treatment reduced considerably the heterogeneity in oxygenation between the two subregions in both tumor models, especially in MDA-MB-468 (Figs. 4F and 4H). Accordingly, analysis of temporal variance showed a significant reduction in sO_2 at the cores of control KPL-4 and MDA-MB-468 tumors, whereas in the bevacizumab group tumor core sO_2 did not vary significantly over the observation period (Supplementary Table S1).

Immunohistochemical analysis of vascularity and oxygenation confirms *in vivo* MSOT/eMSOT imaging data

eMSOT findings were validated by histopathologic examination of tumors harvested immediately after *in vivo* measurements. The overall tissue morphology of KPL-4 tumors is shown in cryosection photographs (Figs. 5D, 5K and Supplementary Fig. S5K). The microvessel distribution in KPL-4 (Figs. 5A, 5H and Supplementary Figs. S5A, S5F) and MDA-MB-468 (Figs. 6A, 6F) tumors revealed by staining against the endothelial marker CD31, shows a fairly good resemblance to the corresponding *in vivo* MSOT images of THb distribution (Figs. 5B, 5I, 6B, 6G and Supplementary Figs. S5B, S5G).

Moreover, the pimonidazole stained areas of KPL-4 (Figs. 5G, 5N and Supplementary Figs. S5E, S5I) and MDA-MB-468 (Figs. 6E, 6J) tumors showed good spatial overlap with the eMSOT-derived core sO_2 distribution in corresponding optoacoustic tumor sections (KPL-4; Figs. 5F, 5M and Supplementary Figs. S5D, S5H, MDA-MB-468; Figs. 6D, 6I). Accordingly, Pearson's correlation analysis of histologic and optoacoustic image pairs revealed a strong and significant negative correlation between pimonidazole-positive hypoxic area fraction (calculated in viable tumor tissue with the vascular rim excluded, as shown in Fig. 6M) and eMSOT-derived intratumoral (core) sO_2 in both KPL-4 (Fig. 6K) and MDA-MB-468 (Fig. 6L) xenografts.

Bevacizumab reduces the microvessel density and hypoxic fraction and increases the necrotic fraction and perivascular coverage in KPL-4 and MDA-MB-468 tumors

Anti-CD31 staining revealed a dramatic reduction in the MVD of both KPL-4 (Fig. 7D) and MDA-MB-468 (Fig. 7H) tumors treated with bevacizumab, as shown in the corresponding CD31-stained magnified micrographs (KPL4; Figs. $5G_1$, $5N_1$ and Supplementary Figs. $S5E_{1\text{-}2}$, $S5I_{1\text{-}2}$, S6B, MDA-MB-468; Figs. $6E_1$, $6J_{1\text{-}2}$ and Supplementary Fig. S6C). Accordingly, KPL-4 and MDA-MB-468 tumors of bevacizumab treated mice displayed significantly lower CD31-positive vascular fraction (VF) compared to controls (Supplementary Figs. S6D, S6E), while an excellent correlation between MVD and VF vascular density metrics was found for both tumor types (Supplementary Figs. S6F-G). In addition, bevacizumab treatment caused a significant reduction in the hypoxic fraction (HF) of KPL-4 (Fig. 7E) and MDA-MB-468 (Fig. 7I) tumors, which is also evident from the noticeable reduction in the intensity and spread of pimonidazole-positive immunofluorescence in KPL-4 (Fig. 5N, Supplementary Fig. S5I) and MDA-MB-468 (Fig. 6J) tumor sections from animals treated with bevacizumab in comparison with vehicle (KPL-4; Fig. 5G, Supplementary Fig. S5E, MDA-MB-468; Fig. 6E). Further immunohistochemical analysis against α-SMA revealed increased pericyte coverage in KPL-4 (Fig. 7F) and MDA-MB-468 (Fig. 7J) tumors of the bevacizumab group, based on quantification of co-localized CD31 and α-SMA fluorescence signals. This is also apparent in the α-SMA stains showing increased association of pericytes with CD31-labeled vessels in KPL-4 tumors of the bevacizumab group (Supplementary Fig. $S5I_2$) compared to controls (Supplementary Fig. S5E_2) which displayed fewer pericytes, only partially attached to the blood vessels.

Furthermore, we observed a higher than 2-fold increase in the necrotic fraction (NF) of KPL-4 (Fig. 7G) and MDA-MB-468 (Fig. 7K) tumors of bevacizumab treated mice. This is also noticeable in H&E stains showing substantially enlarged necrotic cores in bevacizumab treated KPL-4 (Fig. 5J, Supplementary Fig. S5J) and MDA-MB-468 (Fig. 6H) tumors compared to respective controls (KPL-4; Fig. 5C, Supplementary Fig. S5C, MDA-MB-468; Fig.6C). These necrotic areas were characterized by intense eosinophilic and absent hematoxylin (insets; Figs. 5C, 5J, Supplementary Figs. S5C, S5J) and DAPI staining (Figs. 5E, 5L and Supplementary Fig. S5L).

Discussion

Optoacoustic (photoacoustic) imaging has been recently considered as a unique method for label-free imaging of functional tumor vascularization and hypoxia at high spatiotemporal resolution, however technical aspects associated with the different attenuation of photon fluence as a function of depth and wavelength employed, limit the accuracy of the technique and obscure validation. We applied eMSOT, a method that enables substantially improved quantitative estimation of hemoglobin oxygen saturation in MSOT images, in a longitudinal manner to resolve the spatiotemporal heterogeneity of oxygenation and blood volume in two orthotopically implanted breast tumor models (KPL-4, MDA-MB-468) undergoing normal growth or growth inhibition in response to bevacizumab therapy.

Rim-core subregion analysis of eMSOT images revealed the development of steep oxygenation and perfusion gradients from rim to core in growing KPL-4 and MDA-MB-468 tumors of the control group. This finding verifies previous optoacoustic studies showing a rim-core effect (2,44,45) and is reflective of the fact that large blood vessels become more abundant at the tumor-host interface (rim) than in central tumor regions. Interestingly, in control KPL-4 tumors, an abrupt increase in mean whole tumor sO_2 was observed over the first few days of the MSOT imaging time course, after which sO_2 levels plateaued (Fig. 2B). This flare in control KPL-4 tumor sO_2 was not accompanied by concurrent increases in THb (Fig. 2A). Although we do not have a definitive explanation for this finding, a similar increasing trend in KPL-4 tumor oxygenation during this early developmental stage has been observed in previous eMSOT experiments with this tumor model and appears to coincide with parallel increases in vascular rim maturity. It is also plausible that intermittent or transient fluctuations in vascular blood flow and perfusion (cyclic hypoxia) in control KPL-4 tumors might have contributed to the magnitude of the observed increase in sO_2 (particularly on d5 post treatment).

In contrast to vehicle, bevacizumab administration induced an acute and significant drop in mean whole tumor sO_2 in both models that was followed by a gradual elevation in oxygenation after continuous treatment with the drug. The sequential drop and rise in tumor oxygenation observed in our study might explain conflicting results from previous studies showing opposite effects of bevacizumab treatment on tumor oxygenation (see Introduction), as our findings strongly suggest that both hypoxia and improved oxygenation can occur, albeit at different time points over the course of treatment. It is also noteworthy that the recovery in whole tumor sO_2 occurred over a longer period in KPL-4 than MDA-MB-468 tumors (58 versus 11 days), presumably due to the lower microvascular density and growth kinetics of the former.

The overall improvement in intratumoral oxygenation observed in bevacizumab-treated animals was accompanied by a significant and persistent decline in whole tumor THb levels in both tumor models that was mainly driven by the rim subregion. In support of this finding, 3D morphometric analysis of the peripheral functional tumor macrovasculature revealed profound changes in the size and density of the macrovascular network as a response to bevacizumab treatment. On the other hand, intratumoral (core) THb levels were less affected by bevacizumab treatment and in spite of the substantial reduction in MVD, the mean blood volume at the cores of bevacizumab treated tumors was similar to controls. A likely interpretation of this findings is that bevacizumab treatment increases the average blood volume per vessel by improving the functionality and perfusion in surviving vessels.

Another important finding of this analysis was that bevacizumab reduces the spatial heterogeneity in oxygenation over the course of treatment, resulting in considerably improved oxygenation at core tumor regions compared with controls, particularly in the MDA-MB-468 tumor model. This improvement in intratumoral oxygenation might result from a more uniform distribution of blood flow in response to VEGF blockade, as shown in previous preclinical studies (48,49). While the findings on bevacizumab-induced hemodynamic changes are on their own revealing, the wider implication of this study relates to rigorously validating eMSOT for the first time as a method that can accurately study tumor spatial heterogeneity and longitudinal oxygenation patterns in solid tumors. Here, eMSOT data were validated qualitatively and quantitatively by detailed histopathologic analysis against co-registered pimonidazole and CD31 stained whole tumor cryosections. First, we were able to provide reasonable visual correlations between THb signal and CD31 positive vasculature, and demonstrate that the severity and spread of hypoxia revealed by pimonidazole staining were highly correlated to the spatial oxygen saturation patterns resolved by eMSOT. Secondly, the dramatic drop in the hypoxic fraction of bevacizumab treated KPL-4 and MDA-MB-468 tumors shown by quantification of pimonidazole fluorescence is consistent with the significantly improved intratumoral oxygenation detected at the cores of the same tumors by eMSOT. Third, pimonidazole-determined hypoxic tumor fraction was strongly anti-correlated with eMSOT-derived mean core sO_2 values on an individual tumor basis and in both breast cancer models examined, providing thus a direct agreement between histological and optoacoustic estimates of the extent of tumor hypoxia. Furthermore, it is worth pointing out that bevacizumab treatment increased necrosis significantly in both tumor models, presumably due to the reduction of newly formed blood vessels, which starves the tumor of nutrients and oxygen (starvation hypothesis) (50).

The concurrent reductions in tumor blood volume and improvements in intratumoral oxygenation observed in our study may be attributed to the phenomenon of vascular "normalization" which is proposed to induce regression of immature and leaky vessels, along with active remodeling of remaining vessels, improved microcirculation and lower hypoxia (51,52). In support of this hypothesis, we found increased α-SMA positive perivascular coverage in both tumor types treated with bevacizumab in agreement with previous reports (15,23,53), indicating increased vessel maturity and a morphologically "normalized" phenotype. In this context, *in vivo* raster-scanning optoacoustic mesoscopy (RSOM) imaging of tumor microvascular morphology and function (54) could shed further light into the normalizing effects of bevacizumab therapy. Additional insights into the changes in vascular extent and function induced by bevacizumab treatment could be obtained by co-administration of exogenous blood pool contrast agents such as ICG (3,11,55). Accordingly, a recently developed functional optoacoustic technique known as oxygen-enhanced optoacoustic tomography (OE-OT) (3,45) could provide complementary information about the spatial heterogeneity in vascular perfusion, hypoxia and necrosis over the course bevacizumab treatment.

Crucially, our longitudinal eMSOT findings on tumor oxygenation responses to bevacizumab therapy may have direct translational consequences. For instance, our results imply that the responsiveness to combined chemotherapy or radiotherapy could be potentially augmented by careful timing of bevacizumab administration, so as to prevent its early hypoxic/anti-vascular effects and benefit from the improvements in intratumoral oxygenation observed at a later stage along the course of treatment. In this context, our work confirms the use of oxygen saturation (sO_2) as a biomarker of cancer progression and supports its utility for non-invasive clinical evaluation of therapeutic responses to antiangiogenic therapy. Besides the immediate translational implications related to the results on bevacizumab, the rigorous histological validation of eMSOT provided in our work brings the technique a step closer to its clinical application and future studies should address the potential of this imaging method in the clinical breast oncology setting.

In summary, our results demonstrate that longitudinal tracking of tumor oxygenation and functional vascularization using eMSOT can yield a more complete understanding of the complex tumor hemodynamic responses to antiangiogenic agents than single time-point measurements. Overall, our findings suggest that functional eMSOT imaging is likely to play a major part in contemporary preclinical cancer research by enabling non-invasive, longitudinal assessment of treatment outcomes and reducing the need for large animal numbers. Furthermore, eMSOT could in principle be applied on hand-held (clinical) MSOT imaging systems to enable tumor oxygenation assessment in larger animals. Future efforts should aim at confirming our findings in additional animal tumor models relevant to clinical bevacizumab therapy (e.g. colon, lung, brain, etc.), including patient-derived xenografts and transgenic murine models, and in response to different dosage and scheduling protocols.

Acknowledgements

The authors would like to thank Sarah Glasl and Pia Anzenhofer for technical support. We are also grateful to Zakiulah Ali for his contribution to the graphical design of this paper and Qutaiba Mustafa for helpful comments on optoacoustic data analysis.

Author Contributions

Conception and design: V. Ntziachristos, E. Liapis

Development of methodology: V. Ntziachristos, E. Liapis, J. Reber

Acquisition of data: E. Liapis, U. Klemm

Analysis and interpretation of data: E. Liapis, J. Reber, A. Karlas

Writing, review, and/or revision of the manuscript: E. Liapis, V. Ntziachristos, A. Karlas

Administrative, technical, or material support: U. Klemm

Study supervision: V. Ntziachristos, J. Reber, A. Karlas

References

1. Ntziachristos V, Razansky D. Molecular imaging by means of multispectral optoacoustic tomography (MSOT). Chem Rev **2010**;110:2783-94
2. Quiros-Gonzalez I, Tomaszewski MR, Aitken SJ, Ansel-Bollepalli L, McDuffus LA, Gill M*, et al.* Optoacoustics delineates murine breast cancer models displaying angiogenesis and vascular mimicry. Br J Cancer **2018**;118:1098-106
3. Tomaszewski MR, Gehrung M, Joseph J, Quiros Gonzalez I, Disselhorst JA, Bohndiek SE. Oxygen-enhanced and dynamic contrast-enhanced optoacoustic tomography provide surrogate biomarkers of tumour vascular function, hypoxia and necrosis. Cancer Res **2018**
4. Brown E, Brunker J, Bohndiek SE. Photoacoustic imaging as a tool to probe the tumour microenvironment. Dis Model Mech **2019**;12
5. Diot G, Metz S, Noske A, Liapis E, Schroeder B, Ovsepian SV*, et al.* Multispectral Optoacoustic Tomography (MSOT) of Human Breast Cancer. Clin Cancer Res **2017**;23:6912-22
6. Stoffels I, Morscher S, Helfrich I, Hillen U, Leyh J, Burton NC*, et al.* Metastatic status of sentinel lymph nodes in melanoma determined noninvasively with multispectral optoacoustic imaging. Sci Transl Med **2015**;7:317ra199
7. McNally LR, Mezera M, Morgan DE, Frederick PJ, Yang ES, Eltoum IE*, et al.* Current and Emerging Clinical Applications of Multispectral Optoacoustic Tomography (MSOT) in Oncology. Clin Cancer Res **2016**;22:3432-9
8. Knieling F, Neufert C, Hartmann A, Claussen J, Urich A, Egger C*, et al.* Multispectral Optoacoustic Tomography for Assessment of Crohn's Disease Activity. N Engl J Med **2017**;376:1292-4
9. Reber J, Willershauser M, Karlas A, Paul-Yuan K, Diot G, Franz D*, et al.* Non-invasive Measurement of Brown Fat Metabolism Based on Optoacoustic Imaging of Hemoglobin Gradients. Cell Metab **2018**;27:689-701 e4
10. Neuschmelting V, Kim K, Malekzadeh-Najafabadi J, Jebiwott S, Prakash J, Scherz A*, et al.* WST11 Vascular Targeted Photodynamic Therapy Effect Monitoring by Multispectral Optoacoustic Tomography (MSOT) in Mice. Theranostics **2018**;8:723-34
11. Bohndiek SE, Sasportas LS, Machtaler S, Jokerst JV, Hori S, Gambhir SS. Photoacoustic Tomography Detects Early Vessel Regression and Normalization During Ovarian Tumor Response to the Antiangiogenic Therapy Trebananib. J Nucl Med **2015**;56:1942-7
12. Tzoumas S, Nunes A, Olefir I, Stangl S, Symvoulidis P, Glasl S*, et al.* Eigenspectra optoacoustic tomography achieves quantitative blood oxygenation imaging deep in tissues. Nat Commun **2016**;7:12121
13. Olefir I, Tzoumas S, Yang H, Ntziachristos V. A Bayesian Approach to Eigenspectra Optoacoustic Tomography. IEEE Trans Med Imaging **2018**;37:2070-9
14. Ferrara N, Hillan KJ, Gerber HP, Novotny W. Discovery and development of bevacizumab, an anti-VEGF antibody for treating cancer. Nat Rev Drug Discov **2004**;3:391-400
15. Tolaney SM, Boucher Y, Duda DG, Martin JD, Seano G, Ancukiewicz M*, et al.* Role of vascular density and normalization in response to neoadjuvant bevacizumab and chemotherapy in breast cancer patients. Proc Natl Acad Sci U S A **2015**;112:14325-30
16. Dings RP, Loren M, Heun H, McNiel E, Griffioen AW, Mayo KH*, et al.* Scheduling of radiation with angiogenesis inhibitors anginex and Avastin improves therapeutic outcome via vessel normalization. Clin Cancer Res **2007**;13:3395-402
17. Dobosz M, Ntziachristos V, Scheuer W, Strobel S. Multispectral fluorescence ultramicroscopy: three-dimensional visualization and automatic quantification of tumor morphology, drug penetration, and antiangiogenic treatment response. Neoplasia **2014**;16:1-13

18. Savai R, Langheinrich AC, Schermuly RT, Pullamsetti SS, Dumitrascu R, Traupe H*, et al.* Evaluation of angiogenesis using micro-computed tomography in a xenograft mouse model of lung cancer. Neoplasia **2009**;11:48-56
19. von Baumgarten L, Brucker D, Tirniceru A, Kienast Y, Grau S, Burgold S*, et al.* Bevacizumab has differential and dose-dependent effects on glioma blood vessels and tumor cells. Clin Cancer Res **2011**;17:6192-205
20. Borgstrom P, Hillan KJ, Sriramarao P, Ferrara N. Complete inhibition of angiogenesis and growth of microtumors by anti-vascular endothelial growth factor neutralizing antibody: novel concepts of angiostatic therapy from intravital videomicroscopy. Cancer Res **1996**;56:4032-9
21. Yuan F, Chen Y, Dellian M, Safabakhsh N, Ferrara N, Jain RK. Time-dependent vascular regression and permeability changes in established human tumor xenografts induced by an anti-vascular endothelial growth factor/vascular permeability factor antibody. Proc Natl Acad Sci U S A **1996**;93:14765-70
22. Borgstrom P, Gold DP, Hillan KJ, Ferrara N. Importance of VEGF for breast cancer angiogenesis in vivo: implications from intravital microscopy of combination treatments with an anti-VEGF neutralizing monoclonal antibody and doxorubicin. Anticancer Res **1999**;19:4203-14
23. Willett CG, Boucher Y, di Tomaso E, Duda DG, Munn LL, Tong RT*, et al.* Direct evidence that the VEGF-specific antibody bevacizumab has antivascular effects in human rectal cancer. Nat Med **2004**;10:145-7
24. Zhou J, Zhang H, Wang H, Lutz AM, El Kaffas A, Tian L*, et al.* Early prediction of tumor response to bevacizumab treatment in murine colon cancer models using three-dimensional dynamic contrast-enhanced ultrasound imaging. Angiogenesis **2017**;20:547-55
25. Li W, Quan YY, Li Y, Lu L, Cui M. Monitoring of tumor vascular normalization: the key points from basic research to clinical application. Cancer Manag Res **2018**;10:4163-72
26. Ehling J, Lammers T, Kiessling F. Non-invasive imaging for studying anti-angiogenic therapy effects. Thromb Haemost **2013**;109:375-90
27. Gerber HP, Ferrara N. Pharmacology and pharmacodynamics of bevacizumab as monotherapy or in combination with cytotoxic therapy in preclinical studies. Cancer Res **2005**;65:671-80
28. Rapisarda A, Melillo G. Overcoming disappointing results with antiangiogenic therapy by targeting hypoxia. Nat Rev Clin Oncol **2012**;9:378-90
29. McGee MC, Hamner JB, Williams RF, Rosati SF, Sims TL, Ng CY*, et al.* Improved intratumoral oxygenation through vascular normalization increases glioma sensitivity to ionizing radiation. Int J Radiat Oncol Biol Phys **2010**;76:1537-45
30. Lee CG, Heijn M, di Tomaso E, Griffon-Etienne G, Ancukiewicz M, Koike C*, et al.* Anti-Vascular endothelial growth factor treatment augments tumor radiation response under normoxic or hypoxic conditions. Cancer Res **2000**;60:5565-70
31. Myers AL, Williams RF, Ng CY, Hartwich JE, Davidoff AM. Bevacizumab-induced tumor vessel remodeling in rhabdomyosarcoma xenografts increases the effectiveness of adjuvant ionizing radiation. J Pediatr Surg **2010**;45:1080-5
32. Heijmen L, Ter Voert EG, Punt CJ, Heerschap A, Oyen WJ, Bussink J*, et al.* Monitoring hypoxia and vasculature during bevacizumab treatment in a murine colorectal cancer model. Contrast Media Mol Imaging **2014**;9:237-45
33. Rapisarda A, Hollingshead M, Uranchimeg B, Bonomi CA, Borgel SD, Carter JP*, et al.* Increased antitumor activity of bevacizumab in combination with hypoxia inducible factor-1 inhibition. Mol Cancer Ther **2009**;8:1867-77
34. Obad N, Espedal H, Jirik R, Sakariassen PO, Brekke Rygh C, Lund-Johansen M*, et al.* Lack of functional normalisation of tumour vessels following anti-angiogenic therapy in glioblastoma. J Cereb Blood Flow Metab **2018**;38:1741-53

35. Yamaguchi S, Hirata K, Toyonaga T, Kobayashi K, Ishi Y, Motegi H*, et al.* Change in 18F-Fluoromisonidazole PET Is an Early Predictor of the Prognosis in the Patients with Recurrent High-Grade Glioma Receiving Bevacizumab Treatment. PLoS One **2016**;11:e0167917
36. Barajas RF, Krohn KA, Link JM, Hawkins RA, Clarke JL, Pampaloni MH*, et al.* Glioma FMISO PET/MR Imaging Concurrent with Antiangiogenic Therapy: Molecular Imaging as a Clinical Tool in the Burgeoning Era of Personalized Medicine. Biomedicines **2016**;4
37. Yamamoto Y, Tamura R, Tanaka T, Ohara K, Tokuda Y, Miyake K*, et al.* "Paradoxical" findings of tumor vascularity and oxygenation in recurrent glioblastomas refractory to bevacizumab. Oncotarget **2017**;8:103890-9
38. Tamura R, Tanaka T, Miyake K, Tabei Y, Ohara K, Sampetrean O*, et al.* Histopathological investigation of glioblastomas resected under bevacizumab treatment. Oncotarget **2016**;7:52423-35
39. Ueda S, Saeki T, Osaki A, Yamane T, Kuji I. Bevacizumab Induces Acute Hypoxia and Cancer Progression in Patients with Refractory Breast Cancer: Multimodal Functional Imaging and Multiplex Cytokine Analysis. Clin Cancer Res **2017**;23:5769-78
40. Ueda S, Saeki T, Takeuchi H, Shigekawa T, Yamane T, Kuji I*, et al.* In vivo imaging of eribulin-induced reoxygenation in advanced breast cancer patients: a comparison to bevacizumab. Br J Cancer **2016**;114:1212-8
41. Bonekamp D, Mouridsen K, Radbruch A, Kurz FT, Eidel O, Wick A*, et al.* Assessment of tumor oxygenation and its impact on treatment response in bevacizumab-treated recurrent glioblastoma. J Cereb Blood Flow Metab **2017**;37:485-94
42. Higgins B, Kolinsky K, Linn M, Adames V, Zhang YE, Moisa C*, et al.* Antitumor activity of capecitabine and bevacizumab combination in a human estrogen receptor-negative breast adenocarcinoma xenograft model. Anticancer Res **2007**;27:2279-87
43. Xie W, Zhang Y, Zhang S, Wang F, Zhang K, Huang Y*, et al.* Oxymatrine enhanced anti-tumor effects of Bevacizumab against triple-negative breast cancer via abating Wnt/beta-Catenin signaling pathway. Am J Cancer Res **2019**;9:1796-814
44. Rich LJ, Sexton S, Curtin L, Seshadri M. Spatiotemporal Optoacoustic Mapping of Tumor Hemodynamics in a Clinically Relevant Orthotopic Rabbit Model of Head and Neck Cancer. Transl Oncol **2017**;10:839-45
45. Tomaszewski MR, Gonzalez IQ, O'Connor JP, Abeyakoon O, Parker GJ, Williams KJ*, et al.* Oxygen Enhanced Optoacoustic Tomography (OE-OT) Reveals Vascular Dynamics in Murine Models of Prostate Cancer. Theranostics **2017**;7:2900-13
46. Kurebayashi J, Otsuki T, Tang CK, Kurosumi M, Yamamoto S, Tanaka K*, et al.* Isolation and characterization of a new human breast cancer cell line, KPL-4, expressing the Erb B family receptors and interleukin-6. Br J Cancer **1999**;79:707-17
47. Chavez KJ, Garimella SV, Lipkowitz S. Triple negative breast cancer cell lines: one tool in the search for better treatment of triple negative breast cancer. Breast Dis **2010**;32:35-48
48. Tong RT, Boucher Y, Kozin SV, Winkler F, Hicklin DJ, Jain RK. Vascular normalization by vascular endothelial growth factor receptor 2 blockade induces a pressure gradient across the vasculature and improves drug penetration in tumors. Cancer Res **2004**;64:3731-6
49. Dickson PV, Hamner JB, Sims TL, Fraga CH, Ng CY, Rajasekeran S*, et al.* Bevacizumab-induced transient remodeling of the vasculature in neuroblastoma xenografts results in improved delivery and efficacy of systemically administered chemotherapy. Clin Cancer Res **2007**;13:3942-50
50. Folkman J. Anti-angiogenesis: new concept for therapy of solid tumors. Ann Surg **1972**;175:409-16
51. Jain RK. Normalizing tumor vasculature with anti-angiogenic therapy: a new paradigm for combination therapy. Nat Med **2001**;7:987-9
52. Carmeliet P, Jain RK. Principles and mechanisms of vessel normalization for cancer and other angiogenic diseases. Nat Rev Drug Discov **2011**;10:417-27

53. Coutelle O, Schiffmann LM, Liwschitz M, Brunold M, Goede V, Hallek M*, et al.* Dual targeting of Angiopoetin-2 and VEGF potentiates effective vascular normalisation without inducing empty basement membrane sleeves in xenograft tumours. Br J Cancer **2015**;112:495-503
54. Haedicke K, Agemy L, Omar M, Berezhnoi A, Roberts S, Longo-Machado C*, et al.* High-resolution optoacoustic imaging of tissue responses to vascular-targeted therapies. Nat Biomed Eng **2020**;4:286-97
55. Hupple CW, Morscher S, Burton NC, Pagel MD, McNally LR, Cardenas-Rodriguez J. A light-fluence-independent method for the quantitative analysis of dynamic contrast-enhanced multispectral optoacoustic tomography (DCE MSOT). Photoacoustics **2018**;10:54-64

Figure Legends

Figure 1. Experimental methodology and effects of bevacizumab therapy on KPL-4 and MDA-MB-468 tumor growth. **A,** KPL-4 or MDA-MB-468 breast cancer cells were implanted orthotopically into the 3rd thoracic mammary pads of female NOD.SCID mice. **B,** KPL-4 or MDA-MB-468 tumor bearing mice received bevacizumab therapy over the course of weeks. **C,** MSOT scanning of tumors at 21 wavelengths (700-900 nm) and 0.3 mm steps. **D,** Optoacoustic image reconstruction. **E,** eMSOT quantitative mapping of tumor oxygen saturation (sO_2). **F,** Rim-core subregion analysis of oxygen saturation (sO_2) and total hemoglobin concentration (THb), **G,** Cryoslicing, **H,** Immunohistochemistry of tumor cryosections against CD31, pimonidazole and α-SMA. **I-J,** Schematic illustrating MSOT imaging and bevacizumab treatment schemes followed in KPL-4 **(I)** and MDA-MB-468 **(J)** experiments. Tumors of either type were allowed to grow to an average volume of ≈ 200-250 mm^3. MSOT imaging was initiated on d26 (KPL-4) and d21 (MDA-MB-468) p.i. and KPL-4 or MDA-MB-468 tumor bearing mice were imaged at 8 and 5 different time points respectively (black arrows). Bi-weekly treatment with bevacizumab started immediately after the first imaging session at the indicated time points (red arrows). **K-L,** Tumor growth curves for **K,** KPL-4 and **L,** MDA-MB-468 tumors after treatment with vehicle (saline) (black lines) or bevacizumab (red lines). Treatment was initiated on d26 (KPL-4) and d21 (MDA-MB-468) p.i. (red arrows).

Figure 2. eMSOT imaging assessment of spatiotemporal changes in oxygenation and total hemoglobin of KPL-4 tumors during the course of bevacizumab therapy. **A,** total hemoglobin concentration (THb) and **B,** eMSOT oxygen saturation (sO_2) values obtained from KPL-4 tumors of mice treated with either vehicle (black lines) or bevacizumab (red lines) for days 0-58 post treatment. During the time course of bevacizumab treatment average tumor blood volume was progressively reduced, while average sO_2 initially decreased but overall improved by the end of the experiment. **C-D,** Longitudinal changes in THb and oxygenation of a single representative KPL-4 tumor from vehicle **(C)** and bevacizumab **(D)** treatment groups visualized by serial MSOT imaging at 8 consecutive time points. Middle panels: central optoacoustic cross-sections showing THb (800 nm, isosbestic point) distribution. Upper panels: THb maximum intensity projections (THb-MIP). Lower panels: pseudocolorized eMSOT maps of tumor oxygen saturation overlaid on corresponding anatomical images. Color scale bars at the bottom of eMSOT images represent sO_2 levels ranging from 0% (green) to 100% (red). Data are displayed as mean ± SEM (n = 7 mice per KPL-4 treatment group). $^*p < 0.05$, $^{**}p < 0.01$, $^{***}p < 0.001$. Statistical significance between the two treatment groups was assessed by unpaired two-tailed t-test. Scale bar; 2 mm.

Figure 3. Bevacizumab modifies oxygenation and THb dynamics of MDA-MB-468 tumors as revealed by eMSOT imaging. **A,** total hemoglobin concentration (THb) and **B,** eMSOT oxygen saturation (sO_2) values obtained from KPL-4 tumors of mice treated with either vehicle (black lines) or bevacizumab (red lines) for days 0-16 post treatment. Bevacizumab treatment reduced average tumor THb significantly over time, while oxygenation was significantly reduced over the first 5 days of treatment but was restored to control levels by d11. **C-D,** Longitudinal monitoring of spatiotemporal changes in functional vascularization and oxygenation of MDA-MB-468 tumors visualized by 5 serial MSOT images of single, representative tumors from vehicle **(C)** and bevacizumab **(D)** treatment groups. Middle panels: central optoacoustic cross-sections (800 nm, isosbestic point) showing THb distribution. Upper panels: THb maximum intensity projections (THb-MIP). Lower panels:

pseudocolorized eMSOT maps of tumor oxygen saturation overlaid on corresponding anatomical images. Color scale bars at the bottom of eMSOT images indicate sO_2 levels ranging from 0% (green) to 100% (red). Values are reported as mean ± SEM (n = 5 mice per MDA-MB-468 treatment group). $^*p < 0.05$. Statistical significance between the two treatment groups was assessed by unpaired two-tailed t-test. Scale bar; 2 mm.

Figure 4. Rim-core subregion analysis of oxygenation and functional vascularization in KPL-4 and MDA-MB-468 tumor xenografts. KPL-4 and MDA-MB-468 tumors were imaged at 8 and 5 different time points respectively using eMSOT and mean THb and sO_2 values were extracted from tumor rim and core subregions by segmentation analysis (see Methods). **A-D,** Graphical plots showing quantification of mean THb **(A, B)** and sO_2 **(C, D)** at the rim (solid lines) and core (dotted lines) subregions of KPL-4 **(A, C)** and MDA-MB-468 **(B, D)** tumors treated with vehicle (black lines) or bevacizumab (Beva, red lines). Statistical significance between treatment groups in panels A-D was assessed at rim (black asterisks) and core (green asterisks) subregions by unpaired two-tailed t-test. $^*p < 0.05$, $^{**}p < 0.01$, $^{***}p < 0.001$, $^{****}p < 0.0001$. **E-H,** Bar graphs depicting mean sO_2 changes at the rim (black bars) and core (grey bars) subregions of KPL-4 **(E, F)** and MDA-MB-468 **(G, H)** tumor bearing mice treated with vehicle **(E, G)** or bevacizumab **(F, H)** Statistical significance between tumor subregions (black asterisks) in panels E-H was assessed by unpaired two-tailed t-test. $^*p < 0.05$, $^{**}p < 0.01$, $^{***}p < 0.001$, $^{****}p < 0.0001$. Data are displayed as mean ± SEM (n = 7 mice per KPL-4 treatment group, n = 5 per MDA-MB-468 treatment group).

Figure 5. Comparative analysis of histological and optoacoustic data in KPL-4 xenografts. Micrographs of representative whole tumor sections and corresponding optoacoustic slices from control (upper panels) and bevacizumab (lower panels) groups showing: **A, H,** CD31+ microvessel distribution. **B, I,** THb distribution (800 nm, isosbestic point). **C, J,** Upper panels show whole tumor section H&E stains and lower panels show magnified insets of the corresponding regions enclosed in the black dotted rectangles in **(C)** and **(J)**. V; Viable, N; Necrotic. **D, K,** Cryosection photographs. **E, L,** DAPI nuclear stains. **F, M,** Pseudocolorized

eMSOT maps of tumor oxygen saturation overlaid on corresponding anatomical images. Color scale bars on the top of eMSOT images indicate sO_2 levels ranging from 0% (green) to 100% (red). **G, N,** Fluorescence micrographs showing merged pimonidazole (green) and CD31 (red) immunostaining. **G_1, N_1,** magnified views of the white dotted rectangles in (G) and (N) respectively.

Figure 6. Comparative analysis of histological and optoacoustic data in MDA-MB-468 tumors and quantitative immunohistochemical validation of eMSOT-determined intratumoral oxygenation. Representative micrographs of whole tumor sections and corresponding optoacoustic slices of MDA-MB-468 tumors from control (upper panels) and bevacizumab (lower panels) groups showing: **A, F,** CD31+ microvessel distribution. **B, G,** THb distribution (800 nm, isosbestic point). **C, H,** H&E stains. **D, I,** pseudocolorized eMSOT maps of tumor oxygen saturation overlaid on corresponding anatomical images. Color scale bars on the left of eMSOT images indicate sO_2 levels ranging from 0% (green) to 100% (red). **E, J,** Fluorescence micrographs showing merged pimonidazole (green) and CD31 (red) immunostaining. **E_1, $J_{1\text{-}2}$,** magnified views of the white dotted rectangles in (E) and (J) respectively. **K-L,** Pearson correlation analysis of optacoustic and histopathologic data sets showing high inverse correlation coefficients between hypoxic fraction (HF) and eMSOT-derived oxygen saturation (eMSOT-sO_2) at the core of KPL-4 **(K)** and MDA-MB-468 **(L)** tumors. Correlations were assessed on a per-tumor basis from pooled HF/sO_2 measurements from control and bevacizumab treated mice (see Materials and Methods). $^*p < 0.05$. **M,** Exemplary micrograph of a KPL-4 tumor section stained against pimonidazole (left) and binarized image (right) used for calculation of hypoxic fraction (HF). HF was calculated in viable tumor tissue (light green), with the vascular rim (delineated by a red-dotted line) and necrotic (N) areas excluded, as described in detail in Supplementary Methods.

Figure 7. Morphometric and immunohistochemical characterization of tumor vasculature.

A-C, 3D Morphometry of functional tumor macrovasculature. **A,** Maximum intensity projections of THb image stacks (THb-MIP, left panels), extracted tubeness skeleton (middle panels) and labelled skeleton (right panels) of the macrovascular network in KPL-4 tumors treated with vehicle or bevacizumab. Scale bars; 2 mm. **B-C,** Quantitative analysis of total vessel length **(B)** and number of branches **(C)** in the functional macrovasculature of KPL-4 and MDA-MB-468 tumors treated with vehicle or bevacizumab (see Supplementary Methods). **D-K,** quantification of microvessel density (MVD), hypoxic fraction (HF), pericyte coverage and necrotic fraction (NF) in KPL-4 (upper panels) and MDA-MB-468 (lower panels) tumors from control (saline) and bevacizumab treated groups. Bar graphs showing average; **D, H,** CD31+ MVD. **E, I,** pimonidazole positive HF. **F, J,** Pericyte coverage assessed by co-localization analysis of CD31 and α-SMA. **G, K,** Tumor NF. Values are reported as mean ± SEM (n = 6 mice per KPL-4 and n = 4 mice per MDA-MB-468 treatment group). *$p < 0.05$, **$p < 0.01$, ***$p < 0.001$, ****$p < 0.0001$. Statistical significance between the two treatment groups was assessed by unpaired two-tailed t-test.

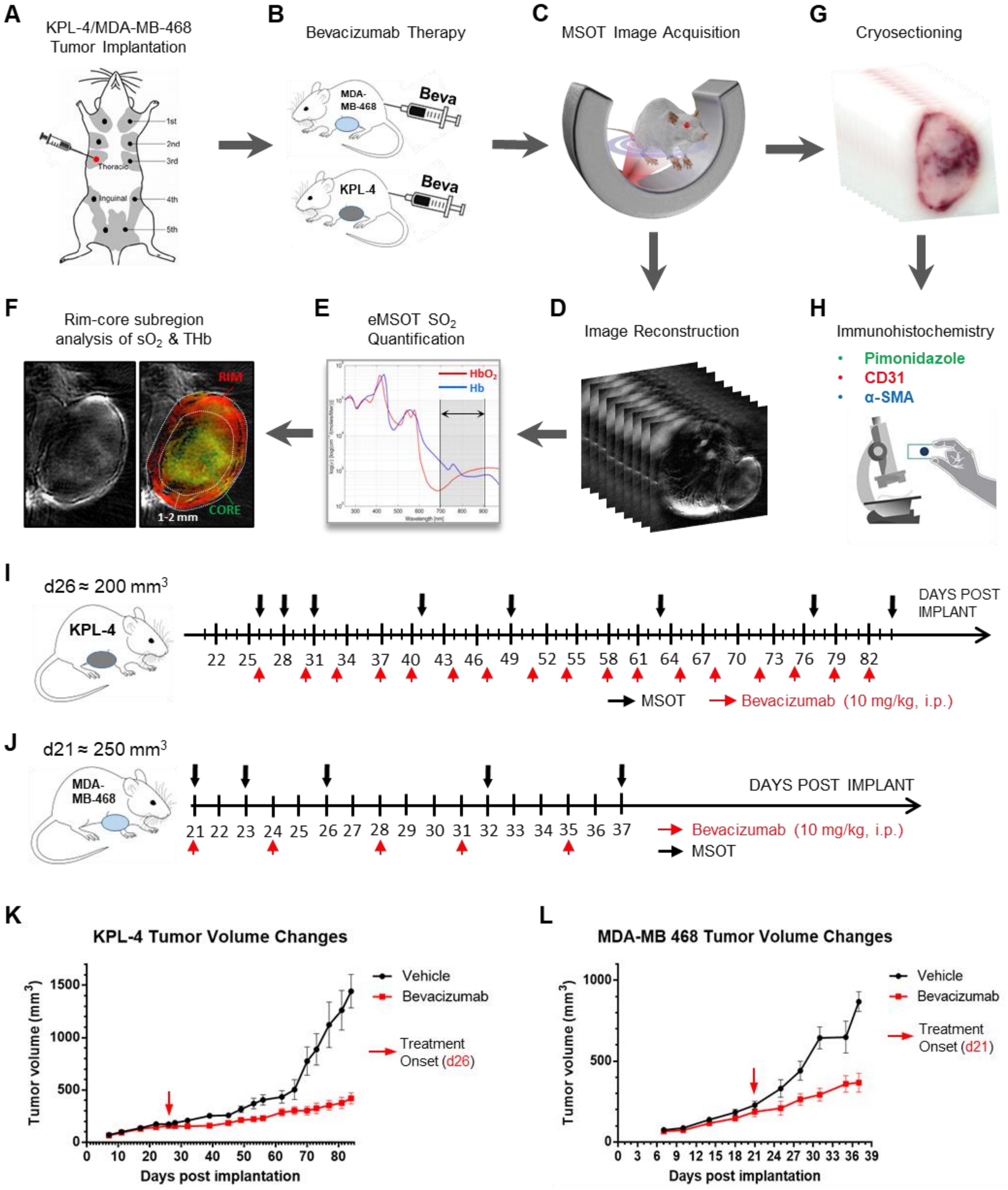
A
KPL-4/MDA-MB-468 Tumor Implantation
1st
2nd
3rd
Thoracic
Inguinal
4th
5th
B
Bevacizumab Therapy
MDA-MB-468
Beva
KPL-4
Beva
C
MSOT Image Acquisition
G
Cryosectioning
F
Rim-core subregion analysis of sO$_2$ & THb
RIM
CORE
1-2 mm
E
eMSOT SO$_2$ Quantification
HbO$_2$
Hb
Wavelength [nm]
D
Image Reconstruction
H
Immunohistochemistry
Pimonidazole
CD31
α-SMA
I
d26 ≈ 200 mm^3
KPL-4
DAYS POST IMPLANT
22 25 28 31 34 37 40 43 46 49 52 55 58 61 64 67 70 73 76 79 82
MSOT
Bevacizumab (10 mg/kg, i.p.)
J
d21 ≈ 250 mm^3
MDA-MB-468
DAYS POST IMPLANT
21 22 23 24 25 26 27 28 29 30 31 32 33 34 35 36 37
Bevacizumab (10 mg/kg, i.p.)
MSOT
K
KPL-4 Tumor Volume Changes
Tumor volume (mm^3)
0
500
1000
1500
0 10 20 30 40 50 60 70 80
Days post implantation
Vehicle
Bevacizumab
Treatment Onset (d26)
L
MDA-MB 468 Tumor Volume Changes
Tumor volume (mm^3)
0
500
1000
0 3 6 9 12 15 18 21 24 27 30 33 36 39
Days post implantation
Vehicle
Bevacizumab
Treatment Onset (d21)

Figure 1

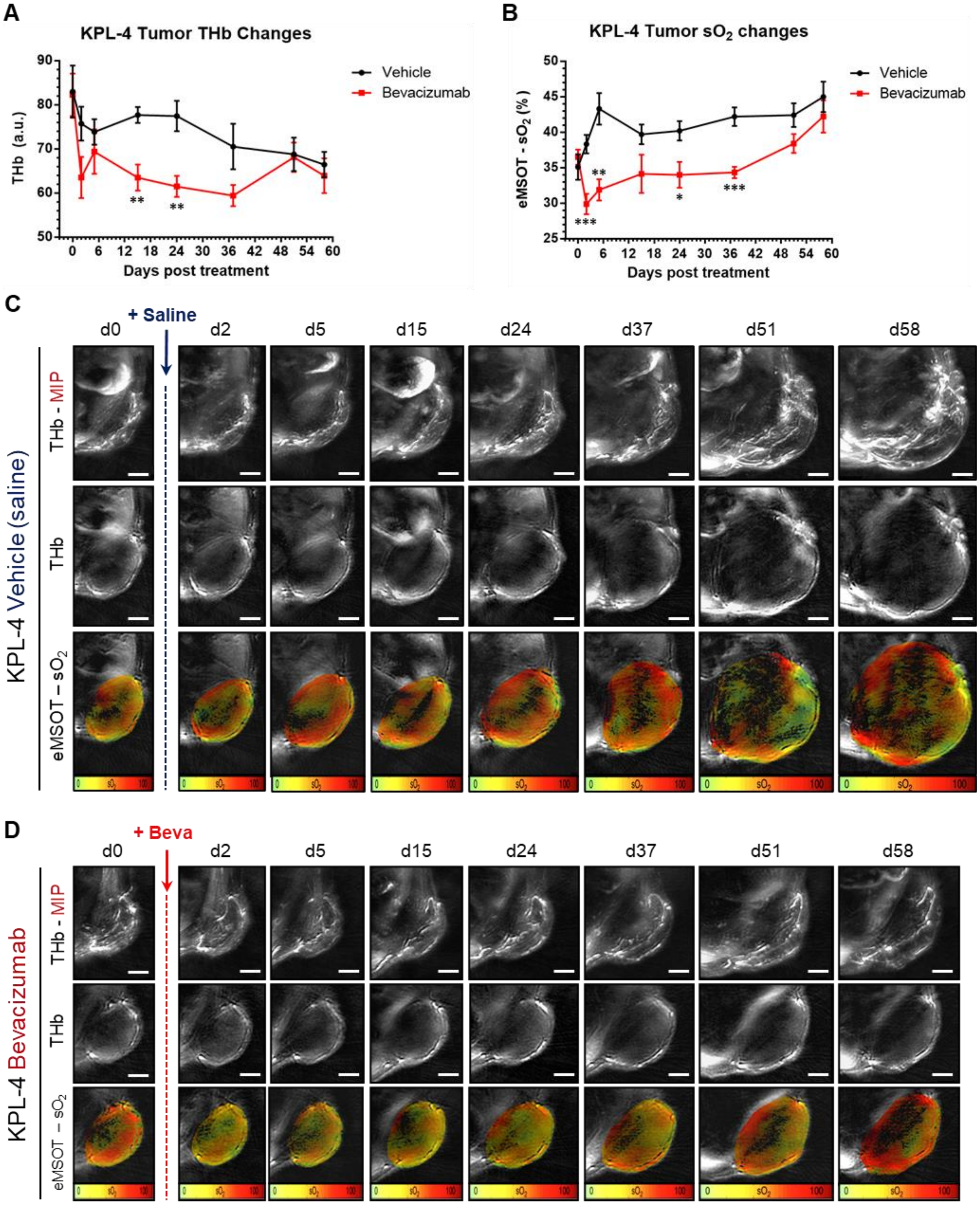
A
KPL-4 Tumor THb Changes
THb (a.u.)
90
80
70
60
50
0 6 12 18 24 30 36 42 48 54 60
Days post treatment
Vehicle
Bevacizumab
**
**
B
KPL-4 Tumor sO_2 changes
eMSOT - sO_2 (%)
50
45
40
35
30
25
0 6 12 18 24 30 36 42 48 54 60
Days post treatment
Vehicle
Bevacizumab
***
**
*
***
C
+ Saline
d0
d2
d5
d15
d24
d37
d51
d58
KPL-4 Vehicle (saline)
THb - MIP
THb
eMSOT – sO_2
0 sO_2 100
D
+ Beva
d0
d2
d5
d15
d24
d37
d51
d58
KPL-4 Bevacizumab
THb - MIP
THb
eMSOT – sO_2
0 sO_2 100

Figure 2

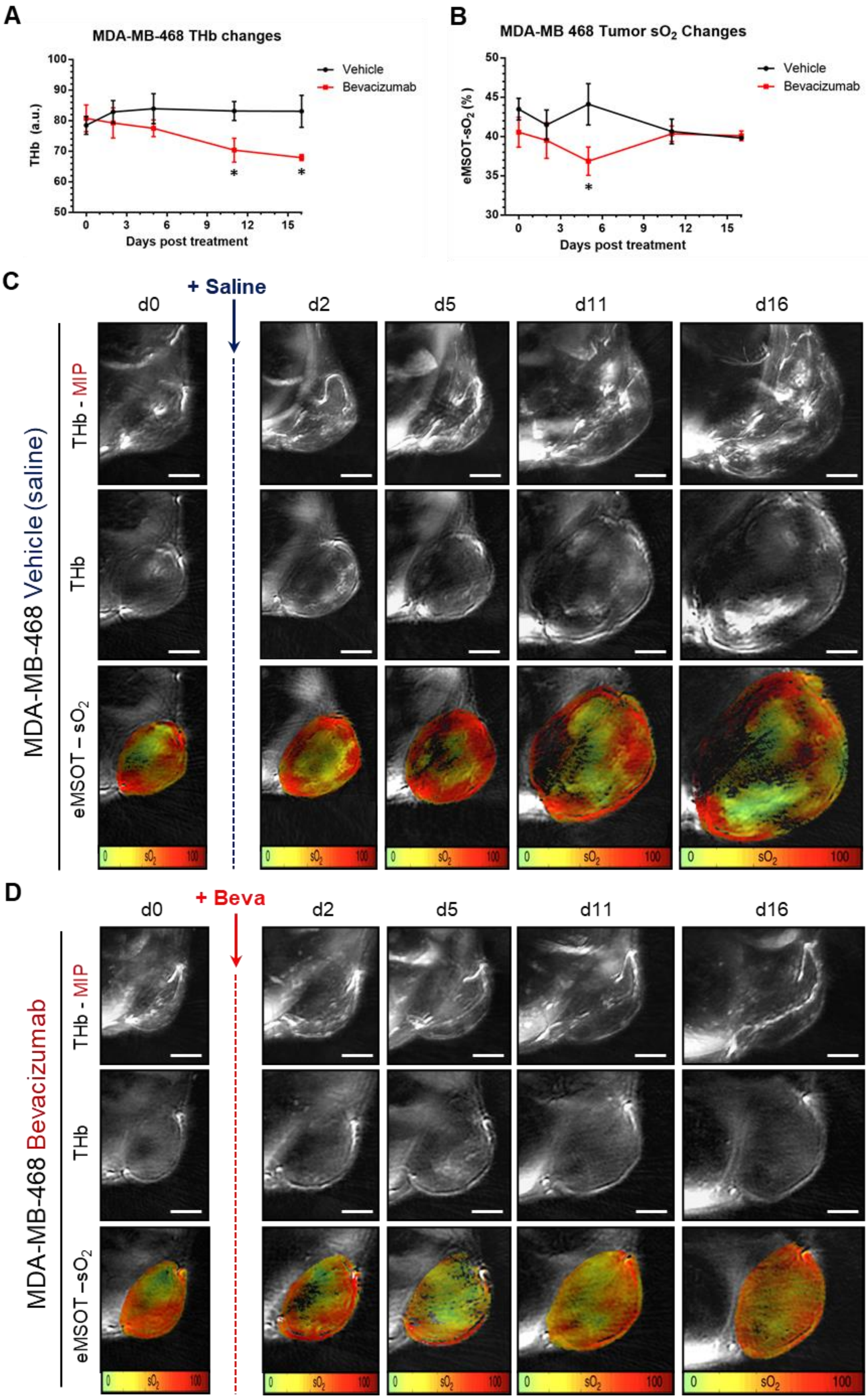
A
MDA-MB-468 THb changes
THb (a.u.)
100
90
80
70
60
50
0
3
6
9
12
15
Days post treatment
Vehicle
Bevacizumab
*
*
B
MDA-MB 468 Tumor sO2 Changes
eMSOT-sO2 (%)
50
45
40
35
30
0
3
6
9
12
15
Days post treatment
Vehicle
Bevacizumab
*
C
+ Saline
d0
d2
d5
d11
d16
MDA-MB-468 Vehicle (saline)
THb - MIP
THb
eMSOT – sO2
0
sO2
100
D
+ Beva
d0
d2
d5
d11
d16
MDA-MB-468 Bevacizumab
THb - MIP
THb
eMSOT –sO2
0
sO2
100

Figure 3

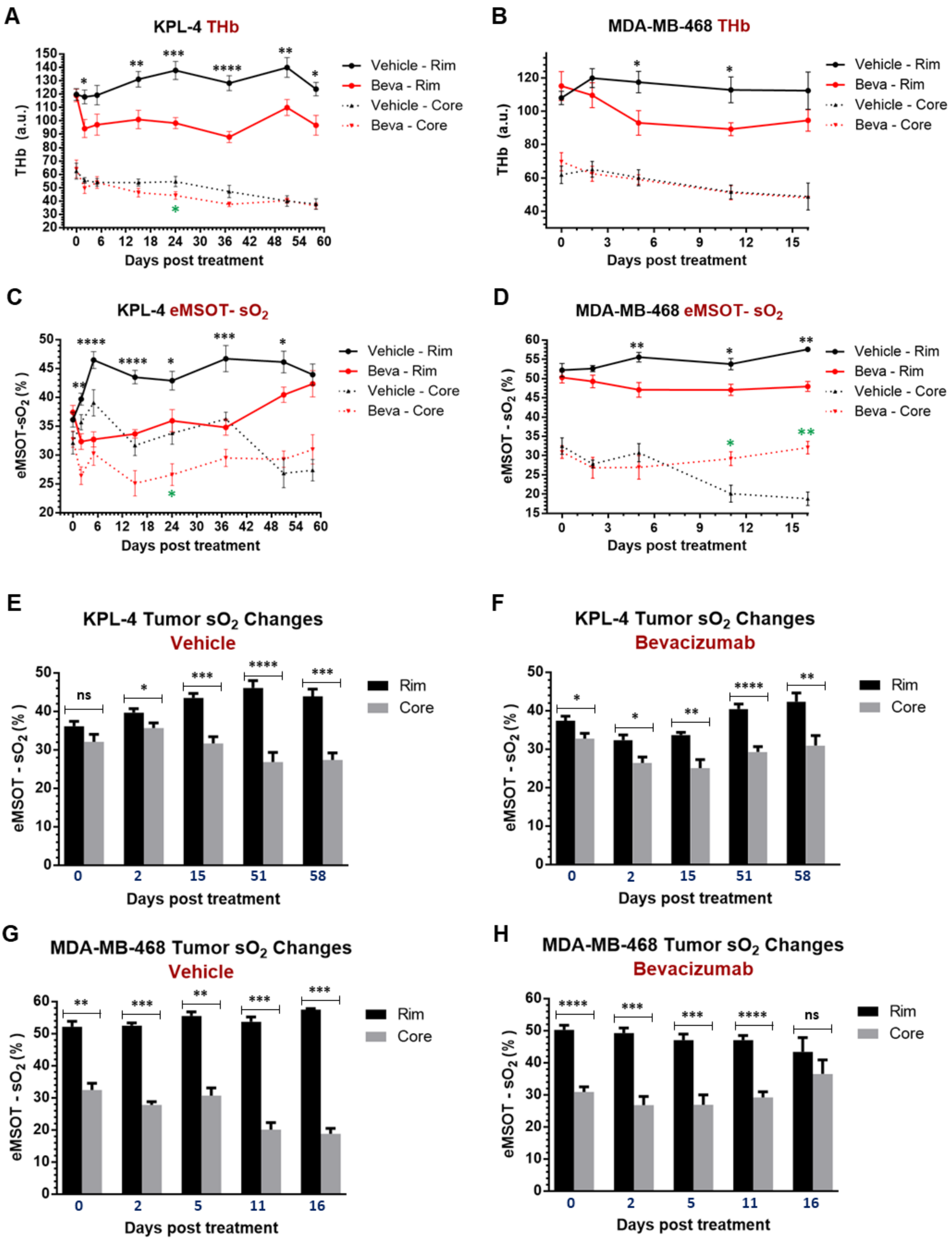
A
KPL-4 THb
THb (a.u.)
150
140
130
120
110
100
90
80
70
60
50
40
30
20
0
6
12
18
24
30
36
42
48
54
60
Days post treatment
*
**
***
****
**
*
*
Vehicle - Rim
Beva - Rim
Vehicle - Core
Beva - Core
B
MDA-MB-468 THb
THb (a.u.)
120
100
80
60
40
0
3
6
9
12
15
Days post treatment
*
*
Vehicle - Rim
Beva - Rim
Vehicle - Core
Beva - Core
C
KPL-4 eMSOT- sO2
eMSOT-sO2 (%)
50
45
40
35
30
25
20
0
6
12
18
24
30
36
42
48
54
60
Days post treatment
**
****
****
*
***
*
*
Vehicle - Rim
Beva - Rim
Vehicle - Core
Beva - Core
D
MDA-MB-468 eMSOT- sO2
eMSOT - sO2 (%)
60
55
50
45
40
35
30
25
20
15
0
3
6
9
12
15
Days post treatment
**
*
**
*
**
Vehicle - Rim
Beva - Rim
Vehicle - Core
Beva - Core
E
KPL-4 Tumor sO2 Changes
Vehicle
eMSOT - sO2 (%)
50
40
30
20
10
0
ns
*
***
****
***
0
2
15
51
58
Days post treatment
Rim
Core
F
KPL-4 Tumor sO2 Changes
Bevacizumab
eMSOT - sO2 (%)
50
40
30
20
10
0
*
*
**
****
**
0
2
15
51
58
Days post treatment
Rim
Core
G
MDA-MB-468 Tumor sO2 Changes
Vehicle
eMSOT - sO2 (%)
60
50
40
30
20
10
0
**
***
**
***
***
0
2
5
11
16
Days post treatment
Rim
Core
H
MDA-MB-468 Tumor sO2 Changes
Bevacizumab
eMSOT - sO2 (%)
60
50
40
30
20
10
0
****
***
***
****
ns
0
2
5
11
16
Days post treatment
Rim
Core

Figure 4

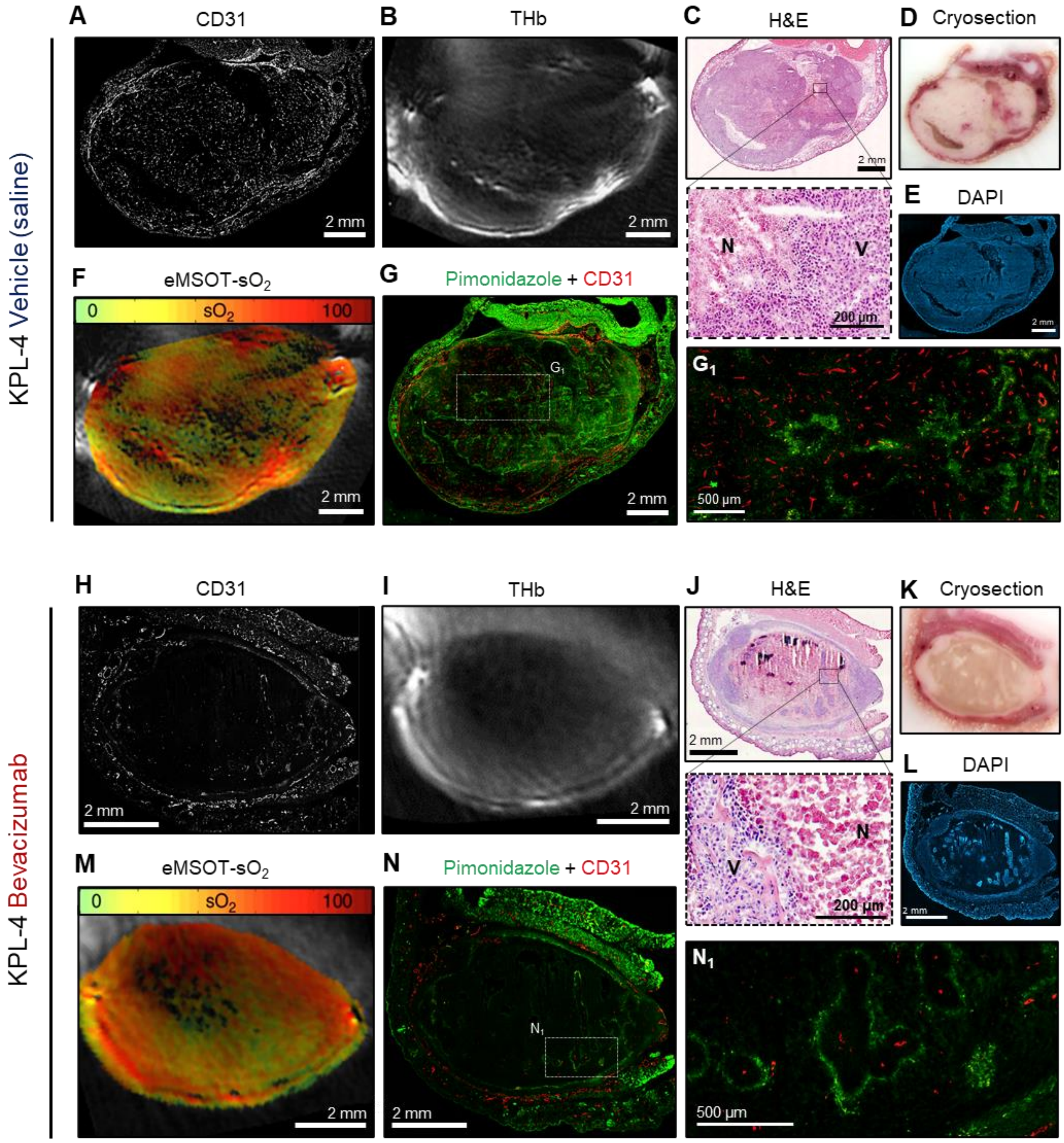
KPL-4 Vehicle (saline)
A
CD31
2 mm
B
THb
2 mm
C
H&E
2 mm
N
V
200 µm
D
Cryosection
E
DAPI
2 mm
F
eMSOT-sO$_2$
0
sO$_2$
100
2 mm
G
Pimonidazole + CD31
G$_1$
2 mm
G$_1$
500 µm
KPL-4 Bevacizumab
H
CD31
2 mm
I
THb
2 mm
J
H&E
2 mm
V
N
200 µm
K
Cryosection
L
DAPI
2 mm
M
eMSOT-sO$_2$
0
sO$_2$
100
2 mm
N
Pimonidazole + CD31
N$_1$
2 mm
N$_1$
500 µm

Figure 5

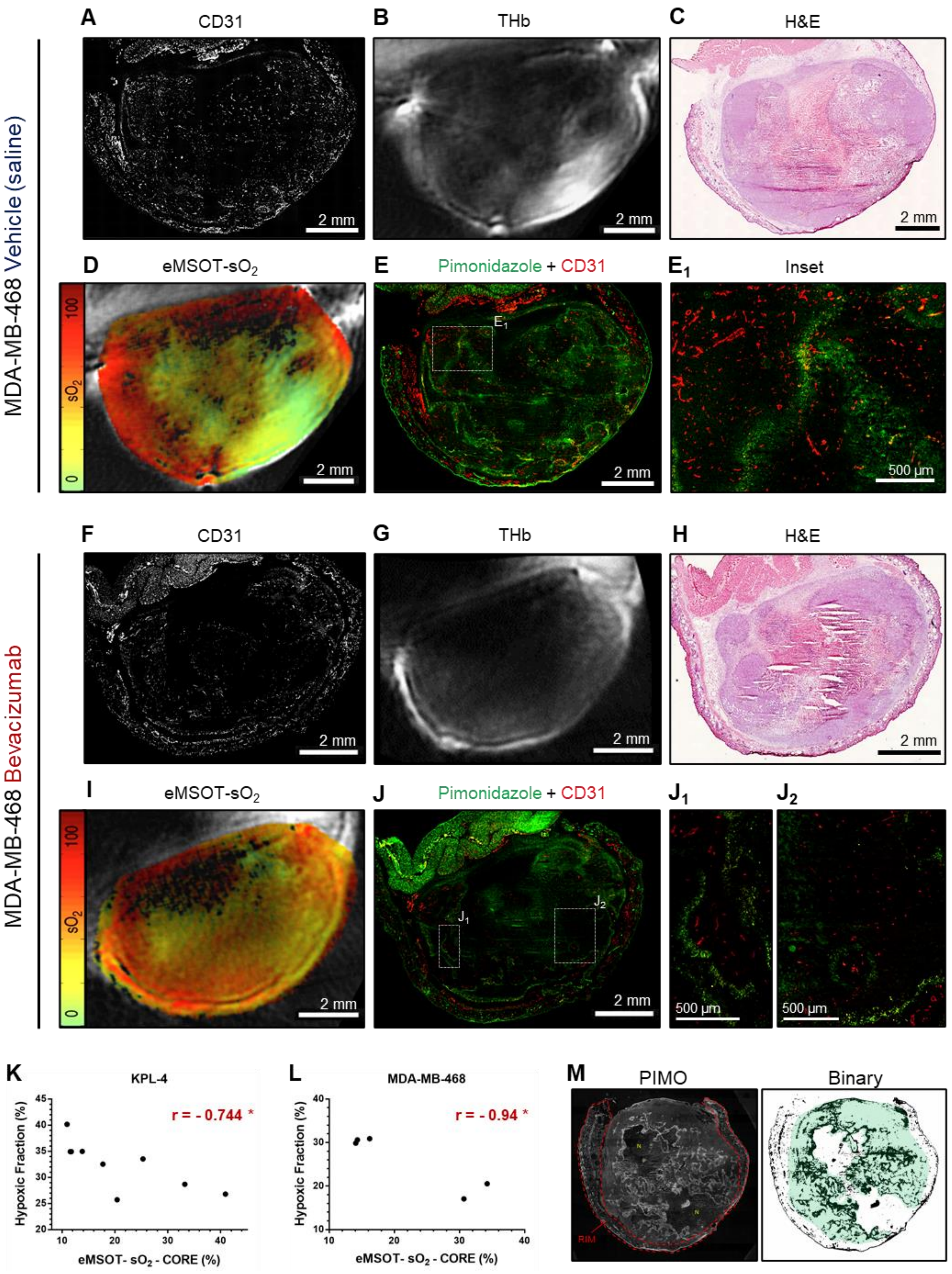
MDA-MB-468 Vehicle (saline)
A
CD31
2 mm
B
THb
2 mm
C
H&E
2 mm
D
eMSOT-sO$_2$
100
sO$_2$
0
2 mm
E
Pimonidazole + CD31
E$_1$
2 mm
E$_1$
Inset
500 µm
MDA-MB-468 Bevacizumab
F
CD31
2 mm
G
THb
2 mm
H
H&E
2 mm
I
eMSOT-sO$_2$
100
sO$_2$
0
2 mm
J
Pimonidazole + CD31
J$_1$
J$_2$
2 mm
J$_1$
J$_2$
500 µm
500 µm
K
KPL-4
r = - 0.744 *
Hypoxic Fraction (%)
45
40
35
30
25
20
10
20
30
40
eMSOT- sO$_2$ - CORE (%)
L
MDA-MB-468
r = - 0.94 *
Hypoxic Fraction (%)
40
30
20
10
10
20
30
40
eMSOT- sO$_2$ - CORE (%)
M
PIMO
N
N
RIM
Binary

Figure 6

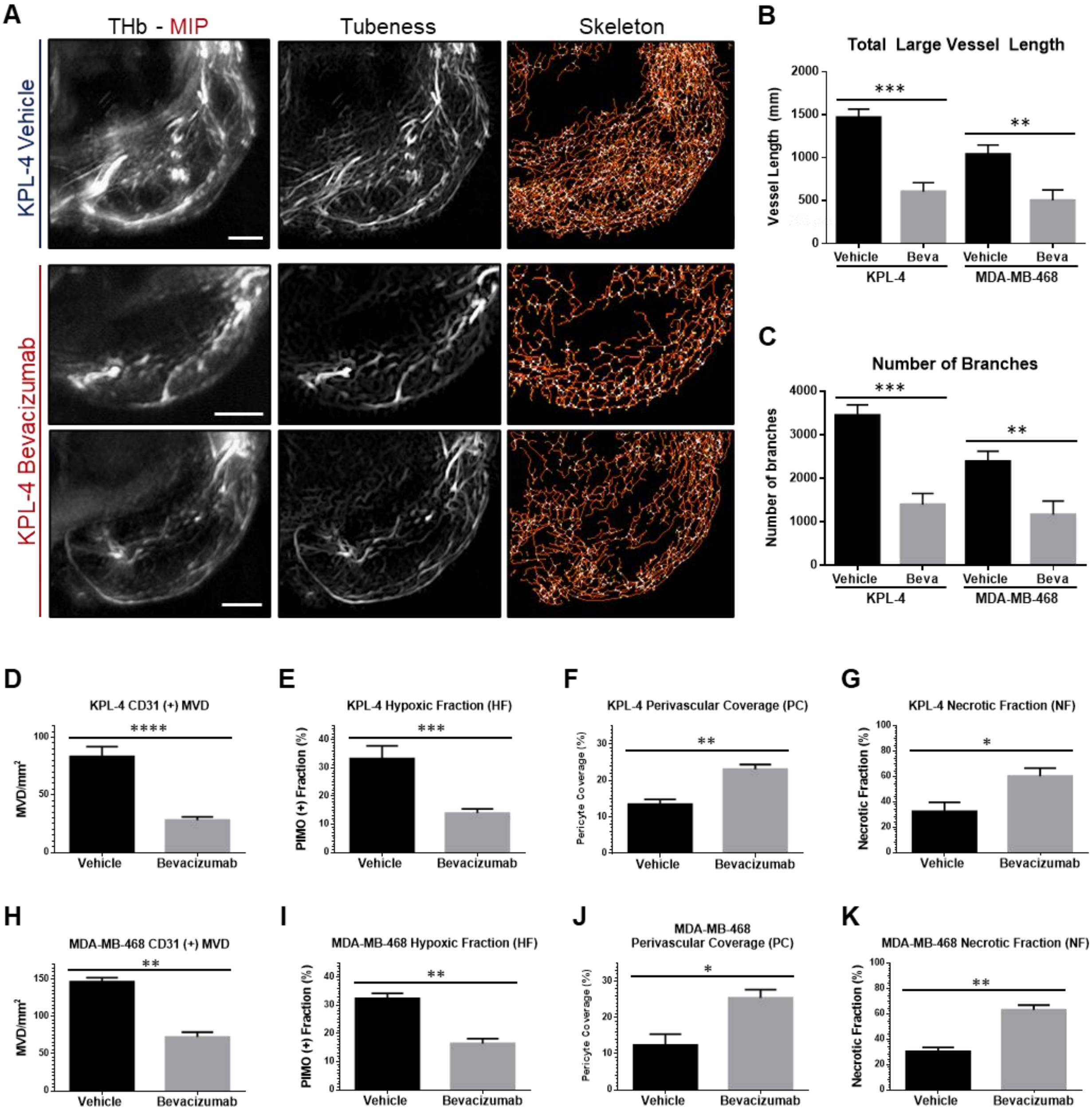
A
THb - MIP
Tubeness
Skeleton
KPL-4 Vehicle
KPL-4 Bevacizumab
B
Total Large Vessel Length
Vessel Length (mm)
2000
1500
1000
500
0
***
**
Vehicle
Beva
Vehicle
Beva
KPL-4
MDA-MB-468
C
Number of Branches
Number of branches
4000
3000
2000
1000
0
***
**
Vehicle
Beva
Vehicle
Beva
KPL-4
MDA-MB-468
D
KPL-4 CD31 (+) MVD
MVD/mm²
100
50
0
****
Vehicle
Bevacizumab
E
KPL-4 Hypoxic Fraction (HF)
PIMO (+) Fraction (%)
40
30
20
10
0
***
Vehicle
Bevacizumab
F
KPL-4 Perivascular Coverage (PC)
Pericyte Coverage (%)
30
20
10
0
**
Vehicle
Bevacizumab
G
KPL-4 Necrotic Fraction (NF)
Necrotic Fraction (%)
100
80
60
40
20
0
*
Vehicle
Bevacizumab
H
MDA-MB-468 CD31 (+) MVD
MVD/mm²
150
100
50
0
**
Vehicle
Bevacizumab
I
MDA-MB-468 Hypoxic Fraction (HF)
PIMO (+) Fraction (%)
40
30
20
10
0
**
Vehicle
Bevacizumab
J
MDA-MB-468
Perivascular Coverage (PC)
Pericyte Coverage (%)
30
20
10
0
*
Vehicle
Bevacizumab
K
MDA-MB-468 Necrotic Fraction (NF)
Necrotic Fraction (%)
100
80
60
40
20
0
**
Vehicle
Bevacizumab

Figure 7

Supplementary Material

Supplementary Methods

Cell lines

The cells were authenticated by the American type culture collection (ATCC) and analysed by several tests for post-freeze viability, morphology, cell growth, interspecies determination and PCR testing of cell culture media for bacterial and fungal contamination, according to the guidelines issued by the national accreditation body for the Federal Republic of Germany (Deutsche Akkreditierungsstelle (DAkkS)). Additional mycoplasma contamination tests were performed using a commercial mycoplasma detection kit (MycoAlertTM, Lonza, Basel, Switzerland). Cells were used for implantation after 3-4 passages following thawing from frozen stocks.

Animals

All procedures involving animal experiments were approved by the Government of Upper Bavaria. All animal experiments were performed in 6-8-week-old, adult female, hairless SHrN® (NOD.Cg-Prkdc^{scid}Hr^{hr}/NCrHsd) NOD.SCID mice (Envigo, Huntingdon, United Kingdom). Animals were housed in experimental animal rooms under specified pathogen-free (SPF) conditions with a 12 h light/dark cycle. The animal rooms are fully air-conditioned, with target values set to 20-24 °C temperature and 45-65% air humidity in accordance with Annex A of the European Convention 2007/526 EG. The maximum stocking densities correspond to Annex III of Directive 2010/63/ EU. If the animals are intolerant, the stocking density is reduced. Cages are equipped with laboratory animal bedding (wood fiber/chips, e.g. Lignocel Select Fine, Rettenmeier). To improve the housing conditions (enrichment), the cages are filled with autoclaved nesting material equipped (mainly nestlets, cardboard houses, pulp). The cages are changed weekly on average, more often in the case of heavy soiling, and less frequently in the case of low soiling or fresh litters in order to disturb the animals as little as possible. The animals received sterile filtered water and a standard diet for rodents (e.g. Altromin 1314) ad libitum. Animals were allowed to acclimate for 1 week prior to experiments. General animal health conditions were monitored daily, signs of distress and body weight were monitored twice weekly and tumor volume 1-2 times per week. Animals were euthanized when tumors reached 1.5 cm in diameter or developed ulceration, in accordance with the termination criteria set by our institute's animal protocol. All experimental procedures were performed under aseptic conditions and in accordance with protocols approved by the Institutional Animal Care and Use Committee. For tumor cell implantation, cells were harvested using 0.05% trypsin, washed and centrifuged in culture medium. KPL-4 cells or MDA-MB-468 were re-suspended in phosphate-buffered saline (PBS) at a concentration of 3×10^6 cells/50 µl and then mixed with 50 µl of growth-factor reduced Matrigel (Corning, NY) to produce a 100 µl 1:1 mixture of PBS and Matrigel. Cell suspensions containing 3×10^6 KPL-4 or 3×10^6 MDA-MB-468 cells were inoculated orthotopically into the right third thoracic mammary fat pad of mice (n = 7 per KPL-4 treatment group, n = 5 per MDA-MB-468 treatment group). All tumor inoculation procedures were completed with the animal anesthetized under isoflurane. KPL-4 and MDA-MB-468 tumors were allowed to grow for 26 and 21 days respectively from the time of implantation when mean volume reached ≈ 200-250 mm^3, after which animals were randomized into control and treatment groups;

1) control group, receiving vehicle (warm saline) injections (i.p., twice weekly), 2) bevacizumab group, treated with bevacizumab (10 mg/kg i.p., twice weekly). All mice survived until the end time points of either imaging experiment (d84 p.i. for KPL-4 and d37 p.i. for MDA-MB-468), except for 2 control KPL-4 tumor-bearing mice that had to be sacrificed at an earlier time point (d77 post implantation) because their tumors reached the maximum allowed size (1.5 cm diameter). Tumor growth was measured in two dimensions using vernier calipers, and tumor volume was calculated using the ellipsoid formula; $V = D \times d^2 \times 0.5$, where D is the longest diameter and d is the perpendicular short diameter. Growth curves were obtained by plotting mean tumor volume against time. Relative tumor volume (RTV) of individual tumors was calculated using the following formula: $RTV = Vx/V1$ where Vx is the volume in mm^3 at the end and V1 at the start of treatment. The percentage tumor growth inhibition (TGI) was calculated as the mean RTV of treated mice/mean RTV of control mice x 100, as in (1). Tumor Growth Delay (TGD) was calculated as T-C, where (T) and (C) are defined as the time in days necessary for a 5-fold increase in tumor volume of the treated (T) and control (C) groups respectively (1).

MSOT imaging of mice

Volumetric optoacoustic imaging was performed using a commercial, real-time whole-body mouse imaging system, MSOT inVision 256-TF (iThera-Medical GmbH, Munich, Germany). The MSOT system and animal preparation procedure have been described in detail previously (2). Briefly, a thin layer of ultrasonic gel (Parker Laboratories Inc., New Jersey, USA) was applied over the tumor region and mice were wrapped into a thin transparent polyethylene membrane (to prevent direct contact of the animal with the water in the imaging chamber) and placed in the animal holder. Following, any remaining bubbles accumulated between the surface of the animal’s skin and the plastic membrane were carefully removed and the holder containing the animal was carefully submerged inside a water bath maintained at 34 °C in order to achieve optimal acoustic coupling and maintain animal temperature while imaging. Mice were allowed to equilibrate their temperature and stabilize their physiology for 10 min within the water bath prior to initiation of MSOT scanning. All imaging procedures were performed under anaesthesia using 2% isoflurane (Zoetis GmbH, Berlin, Germany) delivered in combination with oxygen. Mice were lying in the prone position during scanning. MSOT imaging of KPL-4 tumors was initiated on d26 and of MDA-MB-468 tumors on d21 post implant. KPL-4 tumor-bearing mice were imaged at 8 different time points, on days 26, 28, 31, 50, 63, 77 and 84 post implantation. MDA-MB-468 tumor-bearing mice were imaged at 5 different time points, on days 21, 23, 26, 32 and 37 post implantation. MSOT scanning was performed at 21 wavelengths from 700 to 900 nm with a step size of 10 nm, and 6-35 consecutive slices (depending on tumor size) were acquired for each tumor with a step size of 0.3 mm. MSOT image acquisition was performed by acquiring 10 average frames per wavelength, and therefore, the total duration for acquiring a single multispectral optoacoustic frame was ≈ 26 s. We found 10 averages per wavelength to provide optimal contrast to noise and cardiac/breathing motion compensation, both of which are critical parameters for subsequent eMSOT analysis. Image reconstruction was performed using a model-based inversion algorithm (3,4) with a non-negativity constraint imposed during inversion and with Tikhonov regularization.

eMSOT image processing and data analysis

All optoacoustic image generation and processing was performed using a custom graphical user interface developed in Matlab (Mathworks, MA, USA), that employs the eMSOT algorithm described previously (2). Whole tumor sO_2 and THb content was calculated volumetrically using the entire set of optoacoustic slices from each scan. To calculate the averaged tumor sO_2 values, a region of interest (ROI) encompassing the entire tumor area was manually drawn for each eMSOT image and successively adjusted between consecutive frames. Mean total hemoglobin concentration (THb) was calculated using the 800 nm optoacoustic images which correspond to the isosbestic point of oxy- and deoxyhemoglobin. sO_2 and THb mean intensity values derived from each optoacoustic frame were recorded in excel sheets and averaged and the averaged sO_2 and THb values from all mice of each experimental group (KPL-4; n = 7, MDA-MB-468; n = 5) were calculated and plotted as a function of time. All color maps representing % sO_2 signal were displayed using a color lookup table superimposed on corresponding anatomical (THb) images. In the resulting optoacoustic eMSOT maps, black pixels correspond to areas where the hemoglobin signal was too low to obtain a reliable spectral fitting, and are indicative of necrotic or poorly vascularized/perfused viable tumor regions. The black pixel tumor fraction in eMSOT images varied between 10-20%, according to the developmental stage and size (larger tumors displayed higher fractions than smaller ones), the cross-sectional plane of the tumor examined (central tumor planes exhibited larger fractions than peripheral ones) as well as bevacizumab treatment (bevacizumab treated mice had generally higher fractions than controls). Tumor regions containing such black pixels were excluded from all sO_2/THb calculations. Furthermore, although hemorrhaging was rather infrequent in our tumor models, such hemorrhagic areas were identified on eMSOT images and H&E

stains and excluded from all eMSOT and histologic analyses. All data analysis, including image ROI drawing, was performed blinded until the final statistics were obtained and no outliers were excluded from analysis.

Morphometric analysis of functional macrovasculature

3D morphometric segmentation analysis of the functional macrovascular tumor network was performed using the Tube Analyst macro in imageJ (http://adm.irbbarcelona.org/image-j-fiji). Briefly, 3D MSOT data sets (THb image stacks) of total tumor volumes were contrast-enhanced to eliminate any remaining background noise and analyzed with the macro using the following, empirically determined input parameters: 1) Tube/vessel radius = 7.5 µm, 2) Vessel threshold = 8, 3) Minimal vessel volume = 100 pixels (20.4 pixels/mm). The strong contrast between the macroscopic vessels and the remainder of the tumor enabled the unambiguous segmentation of the rim macrovasculature. The macro yields a Tubeness skeleton (Frangie filter) in addition to a labelled 3D skeleton showing the branching and end-points of connected components. Furthermore, the macro produces a log holding some statistics on the blood vessel network, such as the total length of the network, the number of branches and the overall vascularization density. The values presented in corresponding bar graphs are the average of all tumors analyzed (KPL4; n = 6, MDA-MB-468; n = 4 per treatment group).

Histologic tumor analysis

1. Snap-freezing of excised tumors

Immediately after the last optoacoustic imaging session of each experiment, all animals were treated with the hypoxia marker pimonidazole (Hydroxyprobe Inc., Burlington, MA, USA). Pimonidazole was administered intravenously at 80 mg/kg body weight in a volume of 0.1 ml saline, 1.5 h before the animals were sacrificed. Following, tumors were excised, transferred to pre-labeled cryomolds (Sigma) and embedded in optimal cutting temperature (OCT) compound (Tissue-Tek, Zoeterwonde, NL) to acclimate. At this stage, the tumor was positioned inside the OCT in such way to ensure that the orientation of the tumor was the same as during *in vivo* MSOT imaging. Next, each cryomold was snap-frozen by embedding in – 80 °C isopropanol (Sigma) and stored in a – 80 °C freezer.

2. **Tumor cryosectioning**

   The cryoslicing system consists of a cryotome (CM 1950, Leica Microsystems, Wetzlar, Germany), fitted with a CCD-based detection camera. True color photographic images of the whole body, including the tumor mass, were obtained and 10 µm thick histologic slices derived thereof were thaw-mounted on glass slides. The lower thoracic mouse region containing the tumor was cryosliced in transverse orientation, ensuring that the exact eMSOT imaging plane was aligned with the histological slice.

3. **H&E and immunohistochemical staining of tumor cryosections**

   The cryosections were fixed in in ice-cold acetone for 10 min followed by 3 x 5 min washes in PBS. Then, the tumor sections were blocked with 10% goat serum (in PBS) for 1 h and incubated for 30 min with Crystal A MausBlock reagent (Innovative Diagnostik-Systeme, Hamburg, Germany) at room temperature, washed 3 x 2 min with PBS. Following, the sections were incubated with Crystal B MausBlock reagent (Innovative Diagnostik-Systeme, Hamburg, Germany) for 5 min at room temperature and washed again 3 x 2 min in PBS. Afterwards, the slides were incubated overnight at 4

℃ with mouse MAB1 (1:50, Hydroxyprobe Inc., MA, USA), rat CD31 antibody (1:20, Dianova Research, Hamburg, Germany) and α-SMA (1:100, Abcam) diluted in PBS containing 0.1% BSA plus 1% goat at serum plus 0.1% Tween-20. Subsequently, the slides were washed 3 x 5 min with PBS and then were incubated with AF488 anti-mouse, AF594 anti-rabbit and AF680 anti-rat antibodies (1:500, ThermoFisher Scientific, MA, US) diluted in 1% goat serum for 1 h, at room temperature. Then the slides were washed 3 x 5 min in PBS and mounted with coverslips using Prolong Diamond mounting agent (ThermoFisher Scientific, MA, US). For haematoxylin and eosin (H&E) staining, cryoslices were air dried, fixed in 4% paraformaldehyde (PFA) (Santa Cruz Biotechnology Inc., Dallas, Texas, USA) for 5 min, rinsed with distilled water and incubated 30 s with Haemotoxylin acide by Meyer (Carl Roth, Karlsruhe, Germany) to stain the cell nuclei. The slides were then rinsed in distilled water again before incubation for 1 s in Eosin G (Carl Roth, Karlsruhe, Germany) to stain for protein content. After rinsing in distilled water, the slides were dehydrated in 70%, 94% and 100% ethanol and incubated for 5 min in Xylene (Carl Roth, Karlsruhe, Germany) before being cover slipped with Rotimount (Carl Roth, Karlsruhe, Germany) cover media.

4. Fluorescence microscopy imaging

Representative slides were imaged using a Zeiss Axio Imager M2 microscope fitted with an AxioCam 105 color camera and pictures were then processed using a motorized stitching Zen Imaging Software (Carl Zeiss Microscopes GmbH, Jena, Germany). Fluorescent images were captured under identical conditions (exposure time, scaling) and thresholded to exclude background signal from secondary antibody alone.

Spatial co-registration of optoacoustic and histolopathological data

Registration of THb-CD31 and eMSOT-sO_2-pimonidazole image pairs was performed using the Big Warp plugin in ImageJ (imageJ.nih.gov). Briefly, CD31 and pimonidazole immunostained micrographs were downsampled (maintaining the original aspect ratio) to match the resolution of corresponding THB and eMSOT-sO_2 images respectively. Following, the optoacoustic images were rotated in order to be aligned with the histopathologic stains and image registration was performed by setting landmarks on several different points along the tumor outline in the optoacoustic image (source image) and corresponding points on the histological image (target image) and applying elastic transformation. Transformed optoacoustic images were exported as .tiff images for further image analysis.

Calculation of hypoxic, necrotic and vascular fractions, microvessel density (MVD) and pericyte coverage

Necrotic areas were identified in DAPI nuclear stains and defined as tumor regions with complete absence of DAPI staining including regions with condensed nuclei debris, that were later confirmed in H&E stains as areas characterized by higher eosinophilic staining and absence of hematoxylin staining. Necrotic areas were segmented as regions of interest by hand in ImageJ (imageJ.nih.gov). Tumor necrotic fraction was defined as the surface area of necrotic tissue divided by the total tumor area (excluding the vascular rim). Tumor hypoxia and vascularity were determined by area fraction analysis in ImageJ (imageJ.nih.gov) using manually thresholded, binary pimonidazole- and CD31-stained images. Hypoxic and vascular fractions were calculated as percentages of the positive pimonidazole or CD31 fluorescent area divided by the total vital tumor tissue area, with the necrotic areas excluded. The hypoxic fraction (HF) for each tumor was calculated from 4 central whole tumor sections (with the tumor rim area excluded) per tumor and the values reported in corresponding bar graphs are the average of all tumors analyzed (KPL4; n = 6, MDA-MB-468; n = 4 per treatment group). Microvessel density (MVD) was assessed by fluorescent microscopic analysis of CD31 stained tumor sections using the Weidner method (5), with slight modifications. Briefly, areas of highest neovascularization (neovascular "hot spots") were identified under low (40x) magnification and then individual microvessels were counted on a 100x field equal to 1 mm^2 in area using a calibrated grid. The mean of 4 single 100x fields was computed for each tumor section and results are expressed as the average number of microvessels from 4 central sections per tumor. The vascular fraction (VF) for each tumor was calculated from 4 single 100x fields per slide and values reported represent the average of 4 sections per tumor. For the assessment of pericyte coverage (PC), CD31 and α-SMA co-stained whole tumor cryosections were analyzed at 100x magnification and the degree of pericyte coverage was estimated in ImageJ (imageJ.nih.gov) as the area of co-localized CD31/α-SMA fluorescence signal divided by the overall CD31 positive area. The MVD, VF and PC values reported in corresponding bar graphs are the average of all tumors analyzed (KPL4; n = 6, MDA-MB-468; n = 4 per treatment group).

Supplementary Figure Legends

Supplementary Figure S1.

Weight changes for control (vehicle, black lines) and bevacizumab (red lines) treated **A,** KPL-4 or **B,** MDA-MB-468 tumor-bearing mice. Treatment was initiated on d26 (KPL-4) and d21 (MDA-MB-468) p.i. (red arrows). Values in graphical plots are reported as mean ± SD (n = 7 mice per KPL-4 treatment group, n = 5 per MDA-MB-468 treatment group).

Supplementary Figure S2.

Individual KPL-4 tumor growth retardation and oxygenation changes in response to bevacizumab therapy. **A-B,** Graphical plots showing changes in volume of individual KPL-4 tumors from **A,** control and **B,** bevacizumab treated mice. **C-D,** Graphical plots showing changes in oxygen saturation (eMSOT-sO_2) of individual KPL-4 tumors from **C,** control and **D,** bevacizumab treated mice. **E,** Photographs of KPL-4 tumors of sacrificed mice obtained at the end of this experiment (d84 p.i. – Vehicle; mice #6 and #7 sacrificed on d71 p.i.).

Supplementary Figure S3.

Longitudinal eMSOT imaging of KPL-4 tumors under bevacizumab therapy. **A-B,** Spatiotemporal mapping of changes in vascularity and oxygenation of a single representative KPL-4 tumor from **A,** vehicle and **B,** bevacizumab treatment groups visualized by serial eMSOT imaging at 8 consecutive time points. Middle panels represent central optoacoustic cross-sections (800 nm, isosbestic point) showing THb distribution. Upper panels depict maximum intensity projections (THb-MIP) obtained from single THb optoacoustic sections. Lower panels show pseudocolorized eMSOT maps of tumor oxygen saturation overlaid on corresponding anatomical images. Color scale bars at the bottom of eMSOT images represent sO_2 levels ranging from 0% (green) to 100% (red).

Supplementary Figure S4.

Longitudinal monitoring of spatiotemporal changes in vascularity and oxygenation of MDA-MB-468 tumors using eMSOT. **A-B,** Tumor THb and sO_2 content visualized by 5 serial eMSOT images of single, representative tumors from **A,** vehicle and **B,** bevacizumab treatment groups. Middle panels: central optoacoustic cross-sections (800 nm, isosbestic point) showing THb distribution. Upper panels: THb maximum intensity projections (THb-MIP). Lower panels: pseudocolorized eMSOT maps of tumor oxygen saturation overlaid on corresponding anatomical images. Color scale bars at the bottom of eMSOT images indicate sO_2 levels ranging from 0% (green) to 100% (red).

Supplementary Figure S5.

Comparative analysis of histopathologic and optoacoustic data in KPL-4 xenografts. Micrographs of representative whole tumor sections and corresponding optoacoustic slices from control (upper panels) and bevacizumab (lower panels) groups showing: **A, F,** CD31+ microvessel distribution. **B, G,** MSOT tumor cross-section depicting THb distribution (800 nm, isosbestic point). **C, J,** Left panels show whole tumor section H&E stains and panels on the right show magnified insets of the corresponding regions enclosed in the black dotted rectangles in left panels. **D, H,** pseudocolorized eMSOT maps of tumor oxygen saturation overlaid on corresponding anatomical images. Color scale bars on the left of eMSOT images indicate sO_2 levels ranging from 0% (green) to 100% (red). **E, I,** Fluorescence micrographs showing merged pimonidazole (PIMO, green) and CD31 (red) immunostaining. **E_1, I_1,** magnified views of the respective white dotted rectangles in **(E)** and **(I)**. **E_2, I_2,** magnified views of the corresponding white dotted rectangles in **(E)** and **(I)** showing staining against CD31 (red) and α-SMA (light blue). **K,** cryosection photograph. **L,** DAPI nuclear stain.

Supplementary Figure S6.

Macro- and microvascular changes in bevacizumab treated KPL-4 and MDA-MB-468 tumors. **A,** Maximum intensity projections of the 3D macrovascular network skeleton in KPL-4 (upper panels) and MDA-MB-468 (lower panels) tumors, extracted from THb image stacks of total tumor volumes using the the Tube Analyst macro in imageJ (see Supplementary Methods). Bevacizumab treatment induced a visible reduction in the density and total length of functional tumor macrovasculature. **B-C,** Microvascular "hotspots" revealed by CD31+ endothelial cell immunostaining in KPL-4 **(B)** and MDA-MB-468 **(C)** tumors. Bevacizumab treated tumors (lower panels) display lower MVD compared with tumors treated with vehicle (upper panels). Scale bars; 200 µm. **D-E,** Bar graphs showing CD31+ VF in KPL-4 **(D)** and MDA-MB-468 **(E)** breast tumor xenografts treated with saline (control) or bevacizumab. **F-G,** Pearson correlation analysis of CD31+ microvascular density (MVD) and VF histopathologic data sets in KPL-4 **(F)** and MDA-MB-468 **(G)** tumors showing strong and significant correlation between the two metrics. Correlations were obtained from pooled MVD and VF measurements from control and bevacizumab treated mice (see Materials and Methods). Values are reported as mean ± SEM (n = 4 mice per KPL-4 treatment group). $^{**}p < 0.01$, $^{***}p < 0.001$, $^{****}p < 0.0001$. Statistical significance between the two treatment groups was assessed by unpaired two-tailed t-test.

Supplementary Table Legends

Supplementary Table S1. One-way temporal analysis of variance (ANOVA) of mean THb and sO_2 values at the rim and core subregions of KPL-4 and MDA-MB-468 tumors over the time course of vehicle (control) or bevacizumab treatment. $^*p < 0.05$, $^{**}p < 0.01$, $^{***}p < 0.001$.

Supplementary References

1. Judde JG, Rebucci M, Vogt N, de Cremoux P, Livartowski A, Chapelier A*, et al.* Gefitinib and chemotherapy combination studies in five novel human non small cell lung cancer xenografts. Evidence linking EGFR signaling to gefitinib antitumor response. Int J Cancer **2007**;120:1579-90
2. Tzoumas S, Nunes A, Olefir I, Stangl S, Symvoulidis P, Glasl S*, et al.* Eigenspectra optoacoustic tomography achieves quantitative blood oxygenation imaging deep in tissues. Nat Commun **2016**;7:12121
3. Rosenthal A, Razansky D, Ntziachristos V. Fast semi-analytical model-based acoustic inversion for quantitative optoacoustic tomography. IEEE Trans Med Imaging **2010**;29:1275-85
4. Dean-Ben XL, Ntziachristos V, Razansky D. Acceleration of optoacoustic model-based reconstruction using angular image discretization. IEEE Trans Med Imaging **2012**;31:1154-62
5. Weidner N. Current pathologic methods for measuring intratumoral microvessel density within breast carcinoma and other solid tumors. Breast Cancer Res Treat **1995**;36:169-80